Universiteit Utrecht

Master thesis

Validating the applicability of upwelling and paleotemperature proxies based on long-chain diols in a coastal region (Chile margin) over the last 150 kyr

By: ***Dave Stolwijk BSc*** *– 3404412*

Supervisors: *Prof. dr. ir. S. Schouten & M. de Bar*

Department of Marine Microbiology and Biogeochemistry
NIOZ Royal Netherlands Institute for Sea Research

Faculty of Geosciences
Utrecht University
The Netherlands

Date: 28th of July, 2016

NIOZ Royal Netherlands Institute for Sea Research

Abstract

During the last 10 years, two promising organic proxies based on the relative distribution of long-chain diols have been proposed: the Long chain Diol Index (LDI) and the Diol Index. The LDI is used as a proxy for past sea surface temperatures (SSTs) and the Diol Index can be used to estimate paleoproductivity. Recent application of these paleoenvironmental proxies has yielded promising result, but there are still some uncertainties that obfuscate the definitive application of these long-chain diol based proxies. In this study, a multiproxy approach is used to elucidate part of this uncertainty, related to possible disturbance of the paleoenvironmental signals by river input and extensive upwelling, but also to uncertainty related to interpretation of the Diol Index. Biomarker lipid analysis is performed on core sediments retrieved from ODP site 1234, ~65 kilometer off Concepción, Chile. This area is particularly suitable for this research, because of its proximity to large discharging river systems and its location in the Peru-Chile upwelling system.

The biolipid analysis resulted in several SST and paleoproductivity records, spanning the last ~150 kyr at a resolution of ~2 kyr. The branched isoprenoid tetraether (BIT) index is analysed to assess the impact of terrestrial input on the different diol proxies. However, low BIT values (≤ 0.05) indicate that terrestrial input has been relatively low at ODP site 1234. The LDI SST record is compared with independent records of more established SST proxies based on alkenones and glycerol dialkyl glycerol tetraethers (GDGTs), using the $U^{K'}_{37}$ and TEX_{86}, respectively. The SST records of the three assessed SST proxies agree in terms of main tendencies and amplitudes, with the TEX_{86} generally indicating slightly colder temperatures than the $U^{K'}_{37}$ and LDI. The $U^{K'}_{37}$ SST record most closely resembles the glacial/interglacial temperature trend of the LR04 benthic global stack.

The paleoproductivity proxies assessed during this study, reveal different patterns over the last ~150 kyr. The yielded Diol Index records indicating *Proboscia* paleoproductivity are compared with haptophyte paleoproductivity (based on C_{37} alkenones). While the application of Diol Index 1 seems to be compromised by substantial SST fluctuation over the last ~150 kyr, Diol Index 2 and C_{37} alkenone mass accumulation rate (MAR) indicate increased paleoproductivity rates during the last interglacial. In addition to a productivity peak during marine isotope stage (MIS) 5e, Diol Index 2 indicates a second peak during MIS 5b & 5c. Further research performed at higher resolution is necessary, to more precisely constrain the encountered lag between SSTs and Antarctic atmospheric temperatures and to identify climatic events and possible (sub)millennial oscillation off the Chilean coast.

Table of contents

1. Introduction

Long-chain alkyl diols are lipids which contain alcohol groups at C_1 and at a varying mid-chain position and which were first identified during the early eighties in Black Sea sediments (De Leeuw et al., 1981). Since then, a large variety in long-chain diols has been reported, with chain lengths varying from C_{24} to C_{36}, and mid-chain alcohol positions ranging from C_{11} to C_{19} (Versteegh et al., 1997). Typical long-chain diols in marine sediments are C_{28} and C_{30} 1,13-diols, C_{28} and C_{30} 1,14-diols, and C_{30} and C_{32} 1,15-diols. During the last 10 years, two promising organic proxies for paleoclimate reconstructions have been proposed, based on the relative distribution of these long-chain diols in marine sediments: the Long chain Diol Index (LDI; Rampen et al., 2012) as a proxy for sea surface temperature and the Diol Index (Rampen et al., 2008; Willmott et al., 2010) as a proxy for upwelling/high nutrient conditions.

The LDI is based on the relative distribution of C_{28} and C_{30} 1,13- and 1,15-diols, which shows a good correlation with annual mean sea-surface temperature (SST) in marine surface sediments, suggesting that this index might be useful as a paleotemperature proxy. Although trace amounts of both C_{28} and C_{30} 1,13-diols have been identified in *Proboscia* species (Rampen et al., 2007), it is more likely that they are produced by other autotrophic organisms. The C_{28} and C_{30} 1,13-diols and C_{30} and C_{32} 1,15-diols have been reported to be biosynthesized by upper photic zone inhabiting algae from the class Eustigmatophyceae, in freshwater (Volkman et al., 1999) and marine species (Méjanelle et al., 2003). However, the role of eustigmatophyte algae as a long-chain diol source in marine environments is still uncertain, as the diol distribution found in marine eustigmatophyte algae does not match with the diol distribution found in marine sediments.

The Diol Index is based on the relative abundance of C_{28} and C_{30} 1,14-diols versus 1,13-diols (Wilmott et al., 2010) or 1,15-diols (Rampen et al., 2008). The 1,14-diols, which are widely occurring in the marine water column and sediments, are used as biomarkers for the diatom genus *Proboscia* (Sinninghe Damsté et al., 2003), although the biosynthesis of 1,14-diols has also been reported for the marine heterokont alga *Apedinella Radians* (Rampen et al., 2011). Especially in areas with high primary productivity (PP), such as upwelling areas, the 1,14-diols form a substantial part of the lipid pool (e.g. in the Arabian Sea; Rampen et al., 2008). Coastal upwelling plays a crucial role in regulating the marine organic carbon deposition and the supply of nutrients from the deeper ocean to phytoplankton, thereby modulating atmospheric CO_2 and influencing climate (Ganeshram & Pedersen, 1998). *Proboscia* diatoms thrive best in the early stages of upwelling when nutrient concentrations

strongly increase (Koning et al., 2001) and when the nutricline is shoaling (Rampen et al., 2008). In the more advanced stages of upwelling, the *Proboscia* diatoms are often outcompeted by other organisms (e.g. Chaetoceros; Koning et al., 2001; Herrera & Escribano, 2006). The presence of 1,14-diols is often related to upwelling and considered to be a (paleo)indicator for environments with high PP. The Diol Index can be used to establish the relative importance of *Probosicia* diatoms, by calculating the ratio between '*Proboscia* diols' relative to other diols. Both diol indices are based on chemically similar components and thus likely have similar degradation properties (Rampen et al., 2008). Similar degradation properties for the selected long-chain diols would minimize the influence of diagenetic effects on the paleoproductivity assessment.

Recent applications of the LDI and Diol Index in sediment cores, indicate that the LDI and Diol Index are promising as proxies to constrain paleoenvironmental conditions (e.g. Rodrigo-Gamiz et al., 2014; Plancq et al., 2015; Rampen et al., 2014). However, definitive application of the LDI and Diol Index as valid proxies depends on eliminating obfuscation related to uncertainties associated with these proxies. For instance, De Bar et al. (submitted) showed that for Iberian Atlantic margin surface sediments, the long-chain diol distribution is different in front of major river systems, as compared to the open ocean, which compromises the applicability of the LDI. The LDI proxy gives erroneous results, possibly as a result of the freshwater input, creating conditions in which different organisms proliferate as compared to the rest of the shelf, causing these different diol distributions in the sediment and thereby altering the outcome of the LDI proxy. Rodrigo-Gomez et al. (2015) also found mismatches between the LDI temperatures and *in situ* SSTs around Iceland and attributed this to the low abundance of 1,13- and 1,15-diols and potential contributions of *Proboscia* diatoms to the 1,13- and 1,15 diol pool, limiting the LDI application around Iceland and possibly in other areas where the 1,14-diols strongly dominate the long-chain diol pool. The Diol Index is obfuscated by uncertainty related to the interpretation of this index. Usually, high abundances of *Proboscia* diatoms are associated with upwelling conditions, but previous studies have also related their proliferation with stratified conditions in the water column (e.g. Fernández & Bode, 1994). Similarly, Contreras et al. (2010) have observed increased relative abundance of the C_{28} 1,14-diol at ODP site 1229 (located in the Peru-Chile upwelling system) during the Eemian interglacial (MIS 5e) and have linked this to enhanced water column stratification.

ODP site 1234 provides an excellent study site to constrain the applicability of the LDI and Diol Index, since this site is located in a coastal/deltaic environment which is subject to upwelling conditions. Site 1234 is located in the eastern Pacific Ocean, offshore of

Concepción, Chile, in an upwelling region (Peru-Chile upwelling system). Furthermore, site 1234 lies near the mouths of two major Andean river systems (Río Bio-Bio, Río Itata and their tributaries; Muratli et al., 2010) draining considerable basins. The sediment core from site 1234 covers glacial- and interglacial periods and therefore likely records variations in fluvial input, a factor which could potentially affect the diol distribution (De Bar et al., submitted). Sediment accumulated during interglacial intervals is likely dominated by sediment eroded due to rainfall and river transport, while the sediment eroded during glacial intervals is likely the result of Andean glacier erosion. This makes site 1234 highly suitable to study if variation in fluvial input affects long-chain diol distribution and whether it compromises the long-chain diol proxies. The study area is characterized by relatively high sedimentation rates, thus oxic degradation is not likely to specifically alternate the distribution of diols and other biolipids. Since site 1234 is located in the coastal Peru-Chile upwelling system it also provides the opportunity to test the Diol Index as a recorder of glacial-interglacial variations in upwelling. Furthermore, the Diol Index record can be compared with the record from Contreras et al. (2010), which is obtained from ODP site 1229, located further north. The *Proboscia* paleoproductivity record is also compared with haptophyte algae productivity based on C_{37} alkenones (established haptophyte algae biomarkers; e.g. Volkman et al., 1980). These comparisons could possibly shed more light on the uncertainties associated with the Diol Index.

In this study, the last ~150 kiloyear (kyr) of the sediment core from ODP site 1234 has been sampled and analyzed, with a resolution of ~2 kyr. This time period covers the last glacial (MIS 2-4), the MIS 6 glacial, the current (MIS 1) and the last interglacial (MIS 5; Lisiecki & Raymo, 2005), including the Eemian interglacial (MIS 5e; Shackleton et al., 2002). Late Quaternary sediments were analyzed for long-chain alkenones, glycerol dialkyl glycerol tetraethers (GDGTs) and long-chain diols, in order to establish past SST records based on the $U^{K'}_{37}$ (alkenone unsaturation index; Prahl & Wakeham, 1987), TEX_{86} (TetraEther indeX of tetraethers consisting of 86 carbon atoms; Schouten et al., 2002) and LDI, respectively. This multiproxy approach allows comparison of the LDI-based SST proxy with the more established $U^{K'}_{37}$- and TEX_{86}-based SST proxies, providing a good test for the applicability of the LDI proxy in the region offshore of Concepción, Chile. In addition, more information might be revealed about the ecology (e.g., habitat depth, growing season) of the long-chain diol source organism. The timing of SST changes with respect to climatic changes on Antarctica is assessed by comparison with published $\delta^{18}O$ records. Furthermore, to assess the impact of fluvial input on diol proxies, changes in fluvial input are monitored by the analysis of the

Branched Isoprenoid Tetraether (BIT) index, which is a proxy for fluvially transported terrestrial organic matter (Hopmans et al., 2004).

2. Materials & methods

(2.1) Oceanographic setting ODP site 1234

ODP site 1234 is located in the SE Pacific at ~36°S, ~65 km offshore of Concepción, Chile (*fig. 1*), in an upwelling region and near two major river mouths of the Andean river systems Río Bio-Bio and Río Itata (*fig. 1*), both draining large basins (24,000 km^2 and 11,200 km^2, respectively). Mean annual discharge rates for Río Bio-Bio and Río Itata are 966 m^3/s and 310 m^3/s, respectively, but are subject to highly seasonal flows (Muratli et al., 2010).

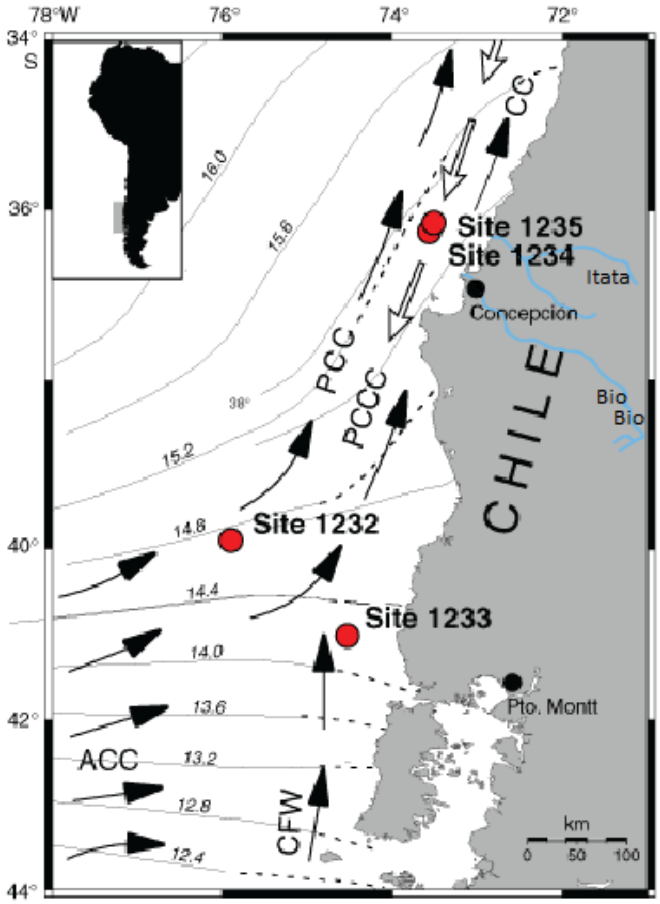

(Fig. 1) Left: *Location of ODP Site 1234, oceanographic features along the Chilean coast (modified from Mix et al., 2003) and nearby discharging rivers. Contours are in degrees Celsius and depict modern mean annual SSTs. The dashed isotherms are extrapolated (after Ocean Climate Laboratory, 1999). (ACC = Antarctic Circumpolar Current, PCC = Peru-Chile Current, PCCC = Peru-Chile Countercurrent, CC = Chile Coastal Current, CFW = Chilean Fjord Water) after Strub et al. (1998) and Lamy et al. (2002). Red dots indicate ODP drilling sites.*

The surface ocean circulation at site 1234 is mainly characterized by the predominantly northward flowing Peru-Chile current (PCC), the Chilean Fjord Water (CFW) and is largely influenced by the Antarctic Circumpolar Current (ACC). These oceanic currents are all part of the Humboldt Current System (HCS), one of the most productive marine ecosystems on earth, which extends from southern Chile up to Ecuador and the Galapagos islands near the equator. The HCS is characterized by a large and dynamic oxygen minimum zone (OMZ) and notable for strong upwelling of cool nutrient-rich subsurface waters of equatorial origin along the coast of Chile. This wind-driven upwelling is the key process responsible for high PP in the HCS (Montecino & Lange, 2009). The predominantly northward flowing surface waters of Antarctic origin and the southeasterly trade winds channeled along the Andes are the driving forces behind the upwelling within the HCS (Thiel et al., 2007). The occurrence of upwelling differs from being mostly continuous in northern Chile, to a more seasonal pattern in southern and central Chile (Thiel et al., 2007). Site 1234 is located in the southern upwelling region of the HCS (*fig. 2*). According to Strub et al. (1998), the seasonal upwelling in the area off Concepción effectuates high biogenic productivity during austral summer, as long as wind directions from south to south-southwest dominate. During austral winter however, coastal upwelling is significantly reduced because wind directions from the north are dominant.

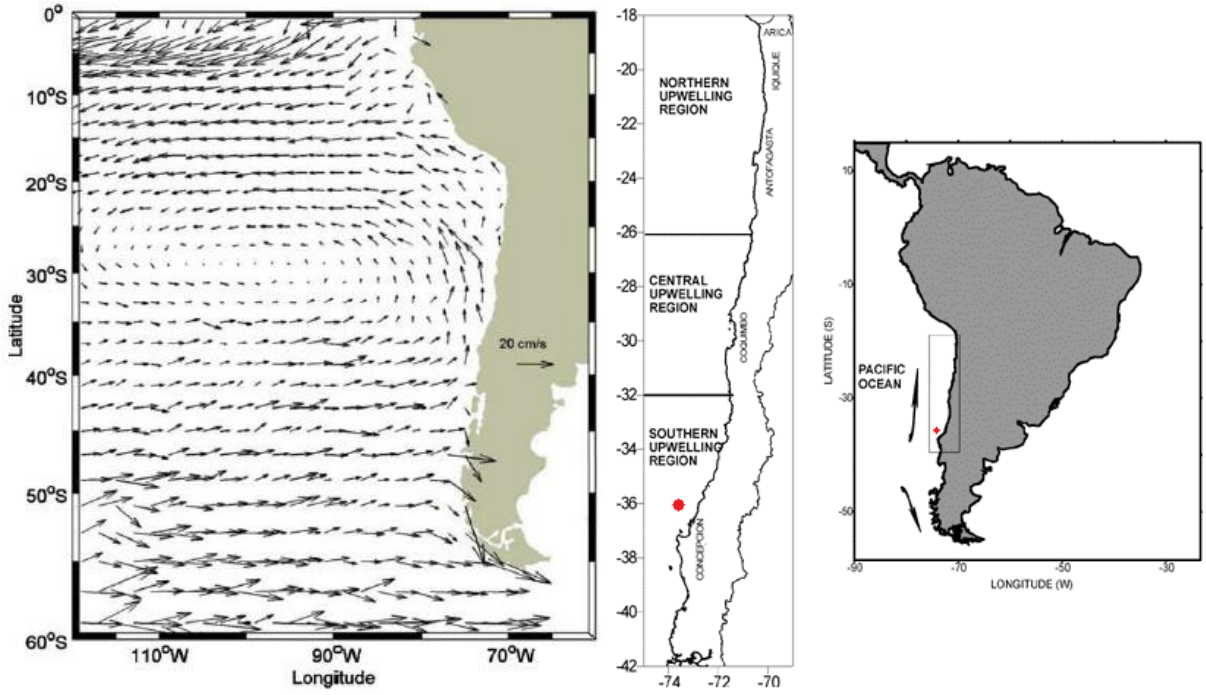

(Fig. 2) ***Left****: Mean surface currents in the SE Pacific, obtained from surface satellite-tracked drifters from 1991 to 2005 (from Montecino & Lange, 2009).* ***Right****: The northern (18 - 26° S), central (26 - 32 °S) and southern (32 - 37° S) upwelling regions in the HCS along the coast of Chile (from Escribano et al., 2004). The red dot represents the location of ODP site 1234.*

The HCS is influenced by the El Niño Southern Oscillation (ENSO) climate signal, which is the result of the coupled interaction between ocean and atmosphere dynamics (Neelin et al., 1998) and is characterized by positive SST and negative sea level pressure anomalies in the eastern Pacific ocean, also known as El Niño anomalies/events (Wang & Picaut, 2004). The ENSO climatic phenomenon is superimposed onto the regional upwelling pattern along the Chilean coast, resulting in large spatial and temporal variety in upwelling intensity, causing ecological disparity in the Chilean coastal waters throughout the years (Thiel et al., 2007). Although the ENSO climatic signal is best known to modulate climatic changes on a interannual-to-decadal time-scale, there seems to be proxy evidence suggesting significant millennial variability that likely involves long-term ENSO changes (Stott et al., 2002). It is even suggested that the ENSO has operated (at least) during the last 130 kyr (Tudhope et al., 2001). The HCS is not only influenced by the ENSO cycle, but also affected by interactions on intra-seasonal (Coastal Trapped Waves [CTWs]; Montecino et al., 2006), annual (Rossby waves; Ramos et al., 2008) and multi-decadal (Pacific Decadal Oscillation; Chavez et al., 2003) time-scales. The interaction of these cycles results in local-scale changes in the depth of the pycnocline and the advection of different water masses into local areas, contributing to the local variability and dynamics of upwelling in the HCS (Montecino & Lange, 2009). Besides the pycnocline, also the thermo-nutricline seems to be a key element controlling the upwelling dynamics of the HCS. Influenced by cold-warm phases at different time-scales (CTWs, the annual seasonal cycle and ENSO), the thermo-nutricline depth changes accordingly, regulating PP by determining the nutrient supply to the euphotic zone. These changes in nutrient supply are felt at every trophic level, causing consequences for prevailing foodwebs (Montecino & Lange, 2009).

(2.2) Sampling & age model

The sediment core from which the samples for this research are taken, was collected during a cruise (ODP Leg 202) with Drilling Vessel *JOIDES Resolution*. Site 1234 (36°13.153´S, 73°40.902´W) is located on a relatively flat bench in the middle of the continental slope, at a water depth of 1015m, located roughly in between the Chilean coast and the Peru-Chile Trench. Ultimately, the drilling recovered a continuous 239-mcd-thick sequence of late Quaternary hemipelagic sediments, presumably primarily terrigenous material provided by rivers (Lamy et al., 2002), with an estimated average sedimentation rate of ~788 m/myr (Initial Reports ODP; Mix et al., 2003).

Sediment samples of approximately 20 cc were taken from the sediment core with plastic scoops, at a resolution of ~2 kyr, covering the last 155 kyr. The age model is derived from Heusser et al., 2006 and based on radiocarbon dates (0-20 kyr before present [BP], calendar corrected using CALIB 5.1) and $\delta^{18}O$ correlations with deep Atlantic core MD95204 (20-75 kyr BP, Shackleton et al., 2000) and the Vostok ice core chronology (75-150 kyr BP, Shackleton et al., 2004). The age model from Heusser et al. (2006) shows a distinct dip in sedimentation rate between ~80 to 90 kyr BP, without a clear explanation by the authors about the presence and origin of this dip. The change in sedimentation rate is relatively large and both starts and ends very abruptly, causing extremely deviating accumulation rates for several organic compound related concentrations, which are normalized to sedimentation rate. In the interval where the age model is causing the supposed age model artefact, the $\delta^{18}O$ age model is comprised of three different records, two of which are originally used in the age model. However, the third $\delta^{18}O$ record seems to reflect a more fluently changing sedimentation rate, without indication of any abrupt changes, but unfortunately does not continue beyond 82.96 kyr BP. Therefore, this $\delta^{18}O$ record (and associated ages) has been used between 0 - 82.96 kyr BP and extrapolated to 90.17 kyr BP, assuming a constant sedimentation rate. This adjustment to the original age model removes the supposed age model artefact. The original age model of Heusser et al. (2006) is applied between 90.17 - 155 kyr BP.

(2.3) Lipid extraction

Seventy-four freeze-dried samples were homogenized with a mortar and pestle. A small fraction of the sample (50-100 mg) was used to measure the total organic carbon (TOC) content, stable carbon isotopes ($\delta^{13}C$) and stable nitrogen isotopes ($\delta^{15}N$). Samples were acidified with 2 M hydrochloric acid (HCl) to remove all carbonates. Decalcified sediments were analyzed with a Thermo Scientific Flash 2000 Elemental Analyzer coupled to a Thermo Scientific Delta V Advantage isotope ratio mass spectrometer. Results were expressed in standard δ-notation relative to Vienna Pee Dee Belemnite (VPDB) for $\delta^{13}C$ and atmospheric N_2 for $\delta^{15}N$ values. The precision as determined using laboratory standards calibrated to certified international reference standards, were in all cases <0.2 ‰ for $\delta^{13}C$ and <0.3 ‰ for $\delta^{15}N$ values. TOC mass accumulation rates (MAR_{TOC}) were estimated for each sample, to take into account the dilution effect by changes in sediment supply. MAR_{TOC} values are based on sedimentation rates (as calculated on basis of the depth-age model from Heusser et al. (2006) derived from $\delta^{18}O$ stratigraphy) and an estimated average gamma ray attenuated (GRA) bulk density of 1,6 g/cm^3.

After addition of extracted diatomaceous earth, the sediments (~15 g dry weight) were extracted using accelerated solvent extraction (ASE), carried out by the DIONEX 200 instrument, at 100 °C and a pressure of 7-8*10^6 Pa, by using a mixture of dichloromethane (DCM) and methanol (MeOH) (9:1; v:v). After obtaining the total lipid extracts (TLEs), each extract was dried under a stream of N_2 within a Caliper TurboVap LV. TLEs that were visually found to contain a substantial amount of elemental sulfur (S_8), were treated with acid-activated elemental copper and DCM to remove the S_8, so that interference of the S_8 with the chromatograph instruments could be prevented. For activation, cupper shavings were placed in an Erlenmeyer flask and submerged in hydrochloric acid (1M). After the cupper turnings reached their typical bright color, the acid was decanted and the cupper turnings were rinsed with bidistilled water (until pH neutral), MeOH and DCM, respectively. The cupper turnings were added to the samples which contained substantial amounts of S_8, stirred overnight with small magnetic stirring bars and subsequently dried over Na_2SO_4, in order to remove the precipitate and remaining H_2O from the TLEs. All samples were dried over anhydrous sodium sulfate (Na_2SO_4) and subsequently dried under a stream of N_2. Before separating the TLEs into different lipid fractions, three standards were added: 10-nonadecanone (C_{19} ketone, 3,008 µg) for alkenones, C_{22} 7,16-diol (4,08 µg) for long-chain diols and the C_{46} GTGT (1 µg) for GDGTs (Huguet et al., 2006). The TLEs (aliquots of ~4.5 mg) were separated into apolar, ketone (containing alkenones) and polar (containing long-chain diols and GDGTs) fractions, by using pipette columns filled with activated (2h at 150 °C) Al_2O_3 and elution with hexane/DCM (9:1; v:v), hexane/DCM (1:1; v:v) and DCM/MeOH (1:1; v:v), respectively. Polar fractions were split for GDGT (25%) and long-chain diol (75%) analysis.

(2.4) Alkenone analysis

The ketone fractions were dried underneath a stream of N_2 and subsequently redissolved in an appropriate amount of ethyl acetate (EtOAc), prior to gas chromatographic analysis. The gas chromatograph (GC) used for the alkenone analysis is an Agilent 6890N GC system. Analysis of the di- ($C_{37:2}$) and tri-unsaturated ($C_{37:3}$) alkenones was done using a 50.0 m Agilent CP7750 capillary column (CP-Sil 5 CB, diameter = 320 µm and film thickness = 0,12µm), with a flame ionization detector and helium as the carrier gas (kept at a constant pressure 100 kPa). Alkenone analysis started with an initial temperature of 70 °C and increased, with a rate of 20 °C/min to 200 °C and subsequently with a rate of 3 °C/min to 320 °C, at which it was held for 25 minutes. The relative abundances of the two different alkenones were determined via the integration of the $C_{37:2}$ and $C_{37:3}$ peak areas. Quantification of the alkenone abundances was achieved by determining the ratio with the added internal standard (IS) peak (representing 4,08 µg). Peak identity was confirmed with a

full scan on a GC coupled to a mass spectrometer (MS). An Agilent 5977A Series GC/MSD, coupled to an Agilent 7890B GC system was used, with a 25.0 m Agilent CP7740 capillary column (CP-Sil 5 CB, diameter = 320 µm and film thickness = 0,12µm) and with helium as the carrier gas, maintaining a constant flow rate of 2 mL/min. Total alkenone MARs were calculated on basis of alkenone concentrations normalized to sedimentation MARs.

Haptophyte algae change their relative proportions of $C_{37:2}$ and $C_{37:3}$ alkenones in response to temperature. At higher temperatures, they biosynthesize a greater relative proportion of the $C_{37:2}$ alkenone. This means that the relative degree of unsaturation of alkenones can be used as a proxy for paleotemperature. To assess the SST on basis of alkenones, the $U^{K'}_{37}$-index (eq. 1) was used (Prahl & Wakeham, 1987):

$$U^{K'}_{37} = \frac{[C37{:}2]}{[C37{:}2] + [C37{:}3]}. \quad (1)$$

The $U^{K'}_{37}$ values where converted to SSTs with the core top calibration of Müller et al. (1998):

$$U^{K'}_{37} = 0.033 \times SST + 0.044. \quad (2)$$

The error of the core top calibration of Müller et al. (1998) is approximately ~1.5 °C. In addition, the produced total alkenone MAR record (mg/m^2/yr) is used as a proxy for productivity. Alkenones are biomarkers for haptophyte algae (Volkman et al., 1980), which can serve as a proxy for haptophyte algae paleoproductivity (Prahl et al., 1988; Brassell et al., 1993).

(2.5) GDGT analysis

After evaporation to dryness under a stream of N_2, the polar fractions (25%) were redissolved in an appropriate amount of hexane : propanol (99:1; v:v), in order to obtain a concentration of ~2mg/mL. The resulting solution was filtered through polytetrafluoroethylene (PTFE) filters with a 0.45 µm pore size. The filtered polar fractions were analyzed for GDGT content by ultra-high-performance liquid chromatography-mass spectrometry (UHPLC/MS) with a Agilent 1260 UHPLC coupled to a Agilent 6130 quadrupole MS in selected ion monitoring (SIM) mode. Two UHPLC silica columns connected in series were used for the GDGT analysis (Waters BEH HILIC columns, 2.1 x 150 mm, 1.7 µm), with an additional pre-column (Waters, 2.1 x 5 mm) of the same material, maintained at 30 °C. The method used for the GDGT analysis, developed by Hopmans et al. (2016), uses A (hexane) and B

(hexane:isopropanol, 9:1; v:v) as the mobile phases. GDGT elution started isocratically for 25 minutes with 18% B, followed by a linear gradient to 35% B in 25 minutes and a linear gradient to 100% B in the 30 min thereafter. The flow rate was kept constant (0.2 mL/min) during the analysis. Conditions for the positive ion atmospheric pressure chemical ionization (APCI)-MS detection in SIM mode of the protonated molecules ($[M + H]^+$) of the various GDGTs were as follows: nebulizer pressure = 60 psi, vaporizer temperature = 400 °C, drying gas = N_2 (constant flow rate of 6 L/min and a temperature of 200 °C), capillary voltage = -3kV, corona = 5 µA (~3.2 kV) (cf. Schouten et al., 2007). The identification and quantification of the GDGT isomers and IS (C_{46} GTGT; 1 µg) was achieved by integrating the peak areas of relevant peaks in *m/z* 1302, 1300, 1298, 1296, 1292, 1050, 1048, 1046, 1036, 1034, 1032, 1022, 1020, 1018 and 744 SIM mass chromatograms. A Drammensfjord sediment standard was used to check for analytical consistency (Schouten et al., 2009). A relative response factor (RRF; see Huguet et al., 2006 for details) value of ~0.57 between the C_{46} GDGT and crenarchaeol, was used to achieve quantification of all encountered GDGTs. To take into account dilution effects related to variation in sediment supply at ODP site 1234, GDGT MARs were ultimately calculated on basis of sediment accumulation rates and GDGT concentrations.

To estimate SSTs on basis of isoprenoid GDGTs, the TEX_{86}^{H} index (eq. 3) was used (Kim et al., 2010), which is defined as the logarithmic function of the original TEX_{86} from Schouten et al. (2002):

$$TEX_{86}^{H} = \log \frac{[GDGT-2] + [GDGT-3] + [Crenarchaeol']}{[GDGT-1] + [GDGT-2] + [GDGT-3] + [Crenarchaeol']}, \quad (3)$$

where numbers correspond with the amount of cyclopentane moieties in isoprenoid GDGTs derived from marine Thaumarchaeota and where Crenarchaeol' refers to the regio-isomer of crenarchaeol (Sinninghe Damsté et al., 2002). The TEX_{86}^{H} values were converted to SSTs with the regional marine and fjord surface sediment calibration of Kaiser et al. (2015) [eq. 4], applicable between 25°S and 50°S off the Chilean coast:

$$SST = 59.6 \times TEX_{86}^{H} + 33.0. \quad (4)$$

The slope of the regional TEX_{86}^{H} surface calibration of Kaiser et al. (2015) is statistically identical to that of the global ocean calibration of Kim et al. (2010), but different in terms of intercept. The calibration of Kaiser et al. (2015) has a standard estimate error of 0.8 °C.

The BIT index is used to measure the amount of river and soil organic matter in sediments and is based on the relative abundance of branched (br) tetraether lipids versus crenarchaeol (Hopmans et al., 2004):

$$\text{BIT} = \frac{[GDGT{-}1] + [GDGT{-}2] + [GDGT{-}3]}{[GDGT{-}1] + [GDGT{-}2] + [GDGT{-}3] + [Crenarchaeol]}, \quad (5)$$

where numbers correspond to the brGDGTs, as described in Hopmans et al. (2004).

(2.6) Long-chain diol analysis

The polar fractions (75% of TLE) were dried under a stream of N_2 and subsequently derivatized by trimethylsilylation of the diols. Polar fractions were redissolved in 25 µL of pyridine and 25 µL of N_2O-bis(trimethylsilyl)trifluoroacetamide (BSTFA) and then heated in an oven at 60 °C for 20 minutes. After the silylation, polar fractions were cooled to room temperature and diluted with 450 µL of EtOAc, resulting in a concentration of roughly 4 mg/mL. Long-chain diol analysis was done on the day of silylation to prevent destabilization of the trimethylsilyl groups, using a GC-MS. The used apparatus and instrument conditions are described in section 2.4. Polar fractions were injected at an oven temperature of 70 °C. The first three minutes, the temperature increased at a rate of 20 °C/min to 130 °C. Thereafter, at a rate of 4 °C/min to the final temperature of 320 °C, at which it was held for 25 minutes. The capillary column was directly inserted into the electron impact ion source of the MSD, with an ionization energy of 70eV. Long-chain diols and the IS were identified in full scan mode (*m/z* range: 50-850) and quantified in SIM mode (*m/z* 187.0 [int. std], 299.4, 313.4, 327.4 & 341.4 [Versteegh et al., 1997]; dwell time = 100 ms). After integration of the relevant peaks, corrections needed to be applied for correct quantification, since each selected ion is representing a fragment of the intact molecule. Selected ion contributions to the total ion counts were (on average): 6.5% for unsaturated long-chain diols, 9.7% for saturated long-chain diols and 19% for the C_{22} 7,16-diol standard (Rodrigo-Gámiz et al., 2015). Total diol MARs were calculated on basis of sedimentation rates, to take into account the dilution effect by changes in sediment supply.

SST assessment on basis of the long-chain diols was achieved by calculating the LDI [eq. 6] and conversion with the corresponding SST equation [eq. 7] from Rampen et al. (2012):

$$\text{LDI} = \frac{[C30\ 1{,}15\ diol]}{[C28\ 1{,}13\ diol] + [C30\ 1{,}13\ diol] + [C30\ 1{,}15\ diol]} \quad (6)$$

$$\text{SST} = \frac{LDI - 0.095}{0.033} \quad (7)$$

The estimated calibration error for the LDI is 2 °C (Rampen et al., 2012). The Diol Indices were calculated, following Rampen et al. (2008) [eq. 8] and Willmott et al. (2010) [eq. 9]:

$$\text{Diol Index 1} = \frac{[C28\ 1{,}14\ diol] + [C30\ 1{,}14\ diol]}{[C28\ 1{,}14\ diol] + [C30\ 1{,}14\ diol] + [\boldsymbol{C30\ 1{,}15\ diol}]} \quad (8)$$

$$\text{Diol Index 2} = \frac{[C28\ 1{,}14\ diol] + [C30\ 1{,}14\ diol]}{[C28\ 1{,}14\ diol] + [C30\ 1{,}14\ diol] + [\boldsymbol{C28\ 1{,}13\ diol}] + [\boldsymbol{C30\ 1{,}13\ diol}]} \quad (9)$$

The 1,13-, 1,14- and 1,15-diol MARs were calculated, to see if changes in the Diol Indices can be attributed to one of these diol concentrations in particular.

3. Results

(3.1) Biomarker analysis

Chromatograms of the extract of one typical sediment are depicted in this section, as an example of the compounds encountered during the biomarker analysis of this study. A typical ketone total ion current (TIC) scan is depicted in *fig. 3*.

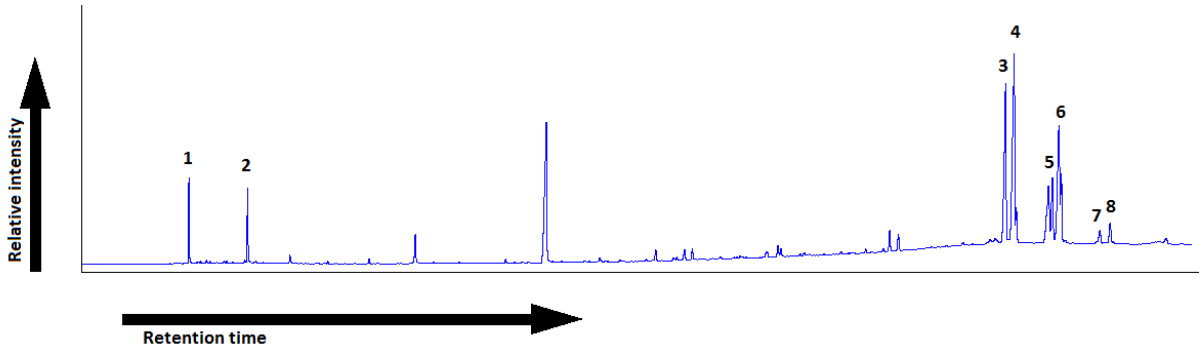

(Fig. 3) *Ketone TIC scan measured with the GC. (**1**) 2-pentadecanone, 6,10,14-trimethyl- (**2**) 10-nonadecanone (C_{19} ketone). (**3**) $C_{37:3}$ alkenone. (**4**) $C_{37:2}$ alkenone. Note that the relative abundance of the less saturated C_{37} alkenone is higher, indicating a relatively high temperature. (**5**) $C_{38:3}$ alkenone. (**6**) $C_{38:2}$ alkenone. (**7**) $C_{39:3}$ alkenone. (**8**) $C_{39:2}$ alkenone.*

Compounds encountered in the ketone TIC scan include unsaturated C_{37}, C_{38} and C_{39} alkenones and contaminants. Peak 1 in fig. 3 (indicating 6,10,14-trimethyl-2-pentadecanone), is e.g. probably related to an oxidation product from plant or vehicular exhaust, formed in the atmosphere as a secondary organic aerosol (Shrivastava et al., 2007).

Fig. 4 depicts a typical base peak chromatogram (BPC) of a polar fraction, measured with UHPLC-MS in SIM mode. The selected *m/z* values (as described in section 2.5) revealed different isoprenoid, branched and hydroxy (OH) GDGTs. The isoprenoid GDGTs are relatively high in abundance, as can be expected for marine sediments, since many marine environments are dominated by the ubiquitous Thaumarchaeota which biosynthesize these isoprenoid GDGTs (Sinninghe Damsté et al., 2002). The peaks that correspond with the brGDGTs, are not visible in the BPC (see *fig. 4*), because their relative abundance is too low compared to the isoprenoid GDGTs. Nevertheless, all known brGDGTs and its isomers, including the recently identified 6-methyl (*m/z* 1050; De Jonge et al., 2013) and 5/6-methyl brGDGTs (*m/z* 1046; Weber et al., 2015) were identified in this study, but not discussed further. In addition to the isoprenoid and branched GDGTs, three OH-GDGTs (0-2 cyclopentane moieties; Liu et al., 2012) have been identified (see *fig. 4*).

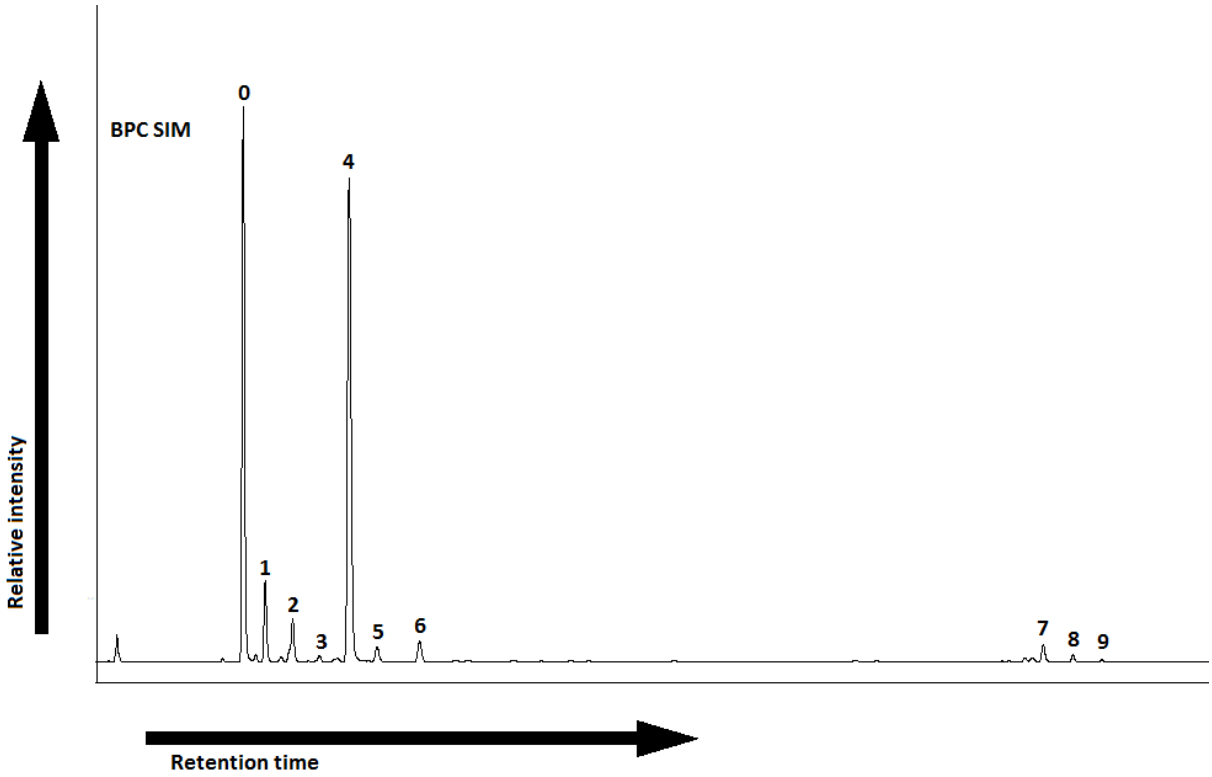

(Fig. 4) *Typical BPC of a polar fraction measured in UHPLC-MS SIM mode. (**0**) GDGT-0. (**1**) GDGT-1. (**2**) GDGT-2. (**3**) GDGT-3. (**4**) Crenarchaeol. (**5**) Regio-isomer crenarchaeol. (**6**) C_{46} GDGT (IS). (**7**) OH-GDGT-0. (**8**) OH-GDGT-1. (**9**) OH-GDGT-2. The brGDGTs elute in between the isoprenoid and OH-GDGTs, however, their relative abundance is too small to be recognized in this chromatogram.*

A typical TIC scan of a polar fraction, measured with GC-MS, is depicted in *fig. 5*, revealing different types of diols, keto-ols, hopanols and other lipids. Worth mentioning are the relatively high abundances of loliolide/isololiolide which are diatom biomarkers that have been reported in sediments underlying highly productive surface waters (Repeta, 1989). The

oleamide peak is a contaminant, which is most probably related to leaching from disposable plastics that were used during the research (McDonald et al., 2008). The SIM traces of the selected ions of diols (depicted in *fig. 6*) revealed the different diols that are present in the recovered sediments. Encountered diols include C_{28} diols (1,12; 1,13 & 1,14), C_{30} diols (1,13; 1,14 & 1,15), the $C_{30:1}$ 1,14-diol and the C_{32} 1,15-diol. At the position in the chromatogram where the C_{31} 1,15-diol would elute (peak 8, *fig. 6*), a clearly observable peak is found in the SIM 327.4 traces of all samples. However, the identity of this diol in full scan was not confirmed. Although a minor amount of this diol could be present, most of this peak is likely related to the C_{31} 17β-21β-hopanol. Also noteworthy, are the remarkably high concentrations of C_{30}, C_{32} and C_{34} keto-ols. In addition to the typical peak pattern depicted in *fig. 6*, occasionally the C_{29} 12-OH fatty acid has been identified, based on characteristic mass spectrum (Versteegh et al., 1997) and relative retention time (Rampen et al., 2009).

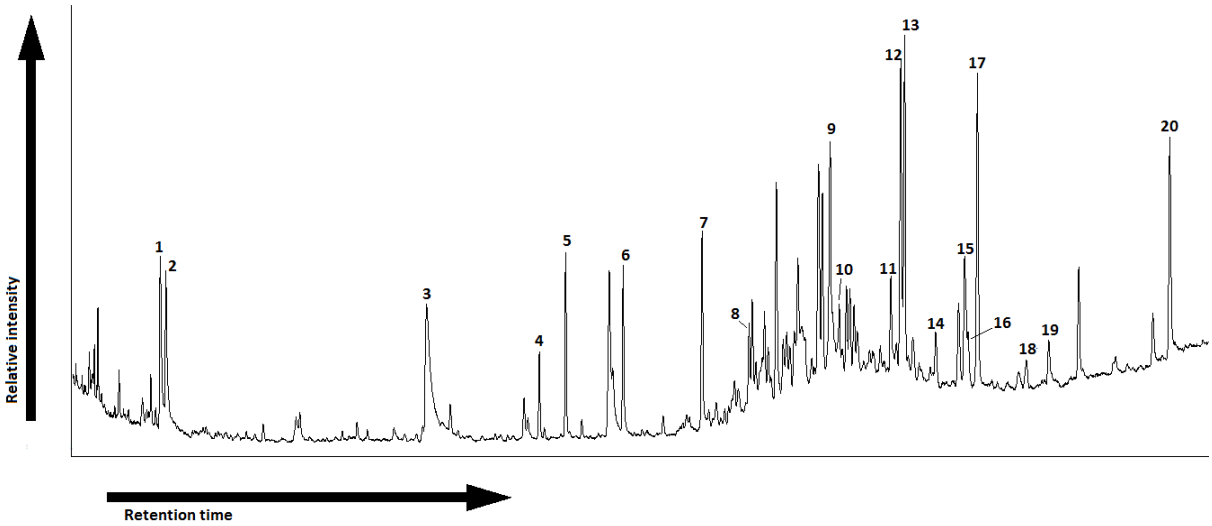

(Fig. 5) *TIC scan of a typical polar fraction measured with GC-MS (m/z range 50-850). (**1**) Isololiolide. (**2**) Loliolide. (**3**) Oleamide. (**4**) 1-Docosanol trimethylsilyl (TMS) ether. (**5**) C_{22} 7,16-diol (IS). (**6**) Tetracosan-1-ol. (**7**) Hexacsoanol. (**8**) Cholesterol. (**9**) Dinosterol. (**10**) C_{28} diols (1,12; 1,13 & 1,14). (**11**) Methyltetradecyl-glycerol diether. (**12**) C_{30} keto-ol. (**13**) C_{30} diols (1,13; 1,14 & 1,15). (**14**) C_{31} 17β-21β-hopanol. (**15**) C_{32} keto-ol. (**16**) C_{32} diols (1,13 & 1,15). (**17**) C_{32} 17β-21β-hopanol. (**18**) C_{34} keto-ol. (**19**) Archaeol. (**20**) Tricyclic biphytane diol (TSM-derivative).*

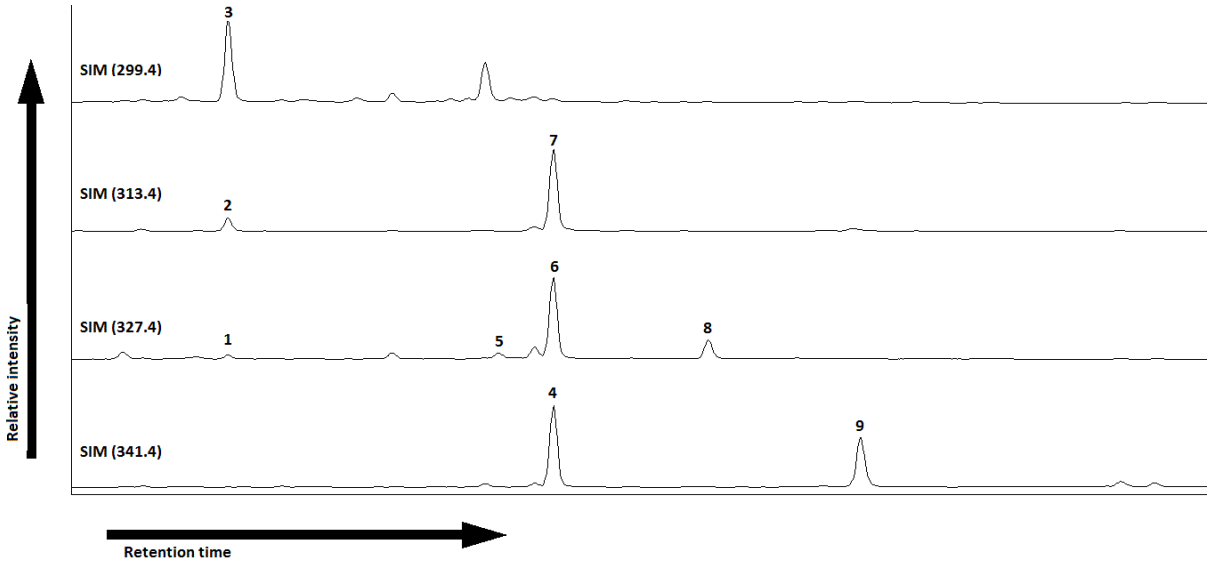

(Fig. 6) *SIM traces of selected m/z values of diols. (**1**) C_{28} 1,12-diol. (**2**) C_{28} 1,13-diol. (**3**) C_{28} 1,14-diol. (**4**) C_{30} 1,13-diol. (**5**) $C_{30:1}$ 1,14-diol. (**6**) C_{30} 1,14-diol. (**7**) C_{30} 1,15-diol. (**8**) C_{31} 17β-21β-hopanol, possibly co-eluting with C_{31} 1,15-diol. (**9**) C_{32} 1,15-diol.*

(3.2) Paleoenvironmental proxies

The abundances encountered during biomarker analysis were high enough to establish paleotemperature and paleoenvironmental records on basis of alkenones, GDGTs and diols. In *fig. 9*, the LR04 benthic $\delta^{18}O$ global stack (*fig. 9A*; Lisieckie & Raymo, 2005) is plotted with the $U^{K'}_{37}$-, TEX^{H}_{86}-, BIT- and LDI-records from this study. The LR04 $\delta^{18}O$ record in the last 150 kyr, is characterized by two rapid deglaciations (during the transition between MIS 6 & 5 and MIS 1 & 2) and a slow glacial build-up between these rapid deglaciations. Below, the individual proxy records are discussed in detail.

(3.2.1) BIT index

The BIT index ranges between 0.02 and 0.05 during the last ~150 kyr BP (*fig. 7C*). Although BIT values are relative stable throughout the time span covered by this study, BIT values are lowest during interglacials (MIS 1 & 5) and are slightly higher during glacial periods (MIS 2, 3 & 6) (significant at the 5% significance level, based on a two-tailed t-Test; p = 0.003. The highest value of 0.05 is observed halfway MIS 4 (63,6 kyr BP), around the time of a minuscule negative excursion in the LR04 $\delta^{18}O$ record (*fig. 7A*).

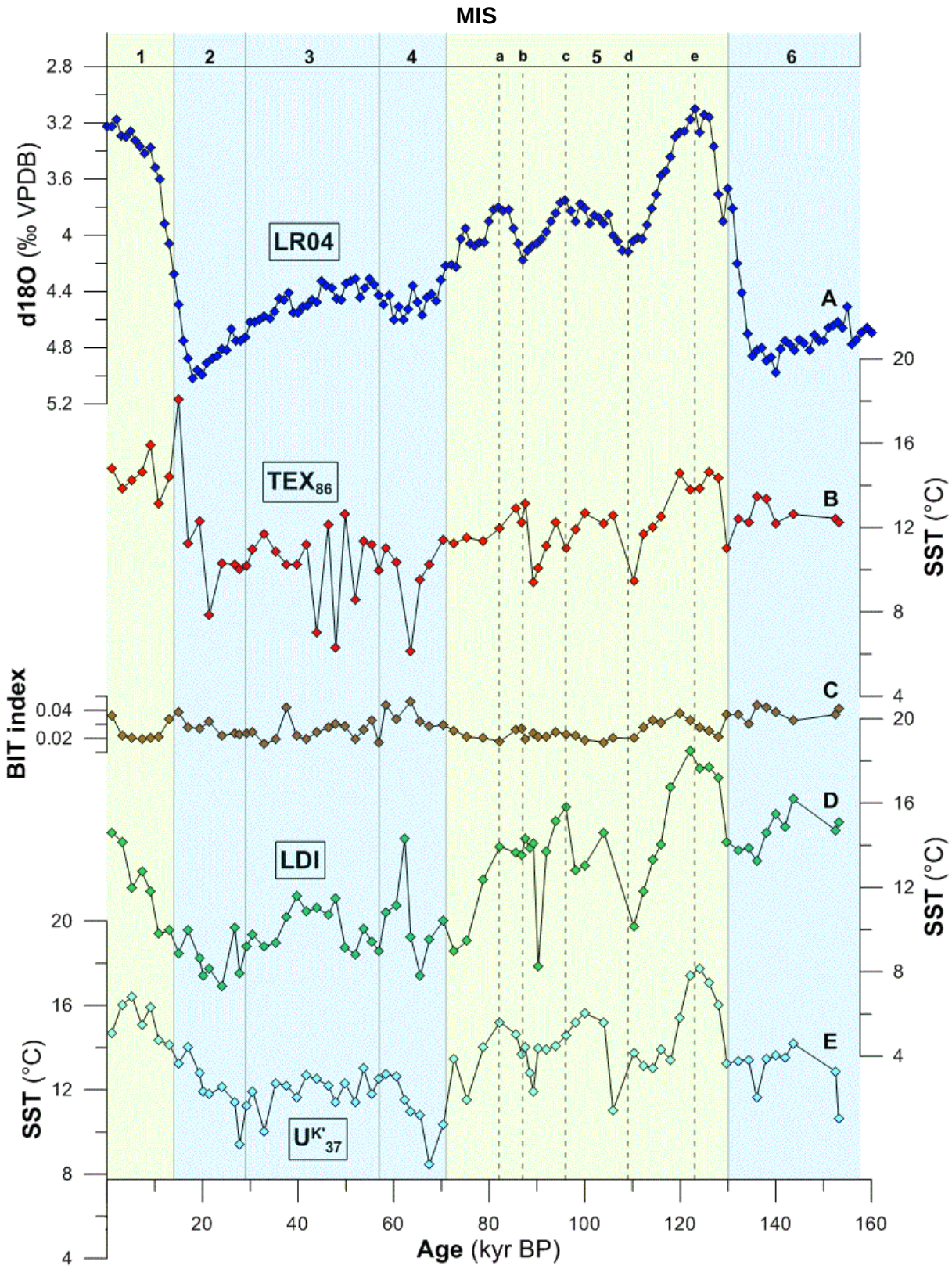

(Fig. 7) Comparison of *SST records and BIT record on basis of different biolipid proxies, from ODP site 1234. (**A**) LR04 benthic $\delta^{18}O$ global stack (Lisieckie & Raymo, 2000), which is shown for reference. Note that the axis is reversed. (**B**) TEX_{86}^{H} SST. (**C**) BIT index. (**D**) LDI SST. (**E**) $U_{37}^{K'}$ SST. MIS stages and substages (ages from Lisciecki & Raymo, 2005) are notified in the top of the figure. Background colors indicate interglacial (green) and glacial (blue) periods. VPDB = Vienna Peedee Belemnite*

(3.2.2) $U_{37}^{K'}$ SST

The late Quaternary $U_{37}^{K'}$ SST record (*fig. 7E*) of ODP 1234 ranges between 8.4 and 17.8 °C. Early in the last interglacial, an increase in temperature is recorded from 13.2 up to 17.8 °C, until the Eemian interglacial maximum (MIS 5e) is reached. The Eemian interglacial (115-130 kyr BP; Dahl-Jensen et al., 2013) is especially well pronounced in the $U_{37}^{K'}$ SST record. In the following ~18 kyr, temperature drops to 11.0 °C near the MIS 5d $\delta^{18}O$ minimum. Subsequently, the recorded temperature rises again until ~15 °C at the peak of MIS 5c, where after temperature drops again to 11.9 °C at the peak of MIS 5b. From there, temperature rises to 15.2 °C, slightly lagging the LR04 $\delta^{18}O$ MIS 5a peak. After this last interglacial substage, a colder temperature regime starts to prevail, leading to a temperature drop of almost ~7 °C, reaching a minimum temperature of 8.4 °C (67.5 kyr BP) in MIS 4, which is the coldest SST of the last ~150 kyr, reached in the ODP 1234 $U_{37}^{K'}$-record. After this SST minimum, the temperature rises to approximately 12 °C, around which SST fluctuates during MIS 3. During MIS 2 a drop to 9.4 °C is observed at 27.8 kyr BP, after which SST gradually rises (though mildly fluctuate) until a present day value of ~15 °C, returning to similar SSTs that occurred during the last interglacial.

(3.2.3) TEX_{86} SST

When TEX_{86}^{H} values are converted to SSTs, the TEX_{86}^{H} temperature record (*fig. 7B*) of ODP 1234 ranges between 6.1 and 18.1 °C. This range is approximately 2.5 °C larger than the $U_{37}^{K'}$ SST range. In addition to this larger range in SST, the temperature record also seems to be interrupted by substantial deviations from the underlying temperature trend, e.g. at 15.0 kyr BP and between 41.8-53.7 kyr BP. Some of these single-point interruptions (in particular at 15.0 and 49.9 kyr BP) show a relative enhanced amount of GDGT-1 and GDGT-2 (up to twice as much in % compared with other sediments). If these deviating values are excluded from the time series, the **Δ**SST approaches that of the $U_{37}^{K'}$-**Δ**SST range.

Starting in the last interglacial, the TEX_{86}^{H} temperature record increases with ~3.5 °C, reaching a peak of 14.6 °C during MIS 5e. It then decreases to 9.5 °C (**Δ**5.1 °C) until the LR04 MIS 5d $\delta^{18}O$ minimum, rises to ~12 °C at the MIS 5c peak (which seems to lead the LR04 global stack slightly), decreases again to 9.4 °C until the MIS 5b minimum, after which a SST peak of ~13 °C is reached during the youngest substage (MIS 5a) of the last interglacial. After the SST peak at MIS 5a, SSTs gradually decrease to a glacial temperature

regime, until SST suddenly drops with 3.4 °C within 2000 years, to a SST of 6.1 °C. This temperature drop could be the representation of the SST drop of MIS 4 $\delta^{18}O$ minimum. The TEX_{86}^{H} temperature record then returns to ~11 °C, similar to pre-single-point excursion SST, where after it enters MIS 3. This isotope stage is characterized by a SST fluctuation with relatively large amplitude, reaching SSTs as low as 6.3 °C and as high as 12.6 °C. TEX_{86}^{H} SST decreases from 11.0 to 7.9 °C in MIS 2, where after it gradually increases (though mildly fluctuates) to the present day value of ~15 °C (ignoring the large spike at 15.0 kyr BP).

(3.2.4) LDI SST

The late Quaternary SST record of ODP 1234 on basis of the LDI (*fig. 7D*), ranges between 7.3 and 18.5 °C. The record is interrupted by two large deviations from the underlying SST trend at 62.4 and 90.3 kyr BP. Early in the last interglacial, the LDI SST record increases with 4.7 °C, from 13.8 to 18.5 °C around the timing of the MIS 5e $\delta^{18}O$ maximum. After the Eemian interglacial, SSTs seem to nearly linearly decrease to 10.2 °C, which is a substantial temperature drop of 8.3 °C. This SST drop is much larger than the 6.8 and 5.1 °C SST drop for the $U_{37}^{K\prime}$- and TEX_{86}^{H} SST records, respectively. After the MIS 5d $\delta^{18}O$ minimum, the LDI SST gradually increases to 15.8 °C at the MIS 5c peak, with a single-point excursion to 14.6 °C, halfway of this gradual increase. SSTs then gradually decrease to 13.7 °C, until an abrupt single-point drop to 8.2 °C, which could be the representation of MIS 5b. Between ~89-82 kyr BP, SSTs seem to be relatively stable (~14 °C), until the shift to the colder glacial regime of MIS 4 occurs, reaching a mimimum of 7.8 °C at 65.6 kyr BP. The LDI SST record then enters a substantially fluctuating episode until reaching relatively stable temperatures of ~11 °C during the middle of MIS 3. SST then drops to a minimum of 7.3 °C in MIS 2, although a noteworthy positive SST excursion of ~2.2 °C takes place just before this minimum temperature is reached. After the SST minimum in MIS 2, the LDI SST record gradually increases to last interglacial-like values, to a present day temperature of ~15 °C.

(3.2.5) Paleoproductivity proxies

In *fig. 8*, different paleoproductivity proxies (total alkenone MAR and the two different diol indices) have been plotted together with TOC_{MAR} and stable carbon and nitrogen isotopes of the organic matter. $\delta^{13}C_{org}$ values (*fig. 8A*) range between -23.0 and -20.4 ‰ throughout the late Quaternary sediment core from ODP site 1234. The mean $\delta^{13}C_{org}$ is significantly lower (~0.6 ‰) during glacial periods compared with interglacial periods (significant at the 5% significance level, based on a two-tailed t-Test; $p < 0.001$). $\delta^{15}N$ values (*fig. 8B*) range between 5.1 and 10.3 ‰ and fluctuate regardless of the glacial/interglacial periods and marine isotope (sub)stages. TOC varied between 0.5 and 3.3 % with a maximum at 82.25 kyr BP, which is slightly before the MIS 5a peak. Mean TOC values are significantly higher (~1 %) during interglacials compared with glacials (significant at the 5% significance level, based on a two-tailed t-Test; $p < 0.001$). To take into account dilution effects regarding the high sedimentation rates estimated for ODP site 1234 (~788 m/myr; Mix et al., 2003), the TOC has been normalized against sedimentation rate and discussed further as MAR_{TOC}. The MAR_{TOC} at ODP site 1234 (*fig. 8C*) ranges between 41.7 and 3.3 gC m^{-2} yr^{-1}. MARs have been largest (~40 gC m^{-2} yr^{-1}) during the last interglacial, between approximately ~105 and ~92 kyr BP. The TOC_{MAR} shows a different pattern than the TOC%, indicating that the TOC_{MAR} has substantially changed over time.

The diol indices of Rampen et al. (2008) and Willmott et al. (2010) produce distinctly different trends. The Diol Index based on 1,14- and 1,13-diols (*fig. 8D*, DI_2; Willmott et al., 2010) ranges between 0.83 and 0.08, with peaks during the last interglacial (between 129.8-114.3 and 100.0-85.61 kyr BP) and smaller peaks around 29.2 and ~142 kyr BP. The Diol Index based on 1,14- and 1,15-diols (*fig. 8E*, DI_1; Rampen et al., 2008) ranges between 0.86 and 0.63, but in contrast to the DI_2 , this record does not seem to indicate very distinct peaks in the last interglacial. E.g. where the DI_2 clearly peaks within MIS 5e, DI_1 records a relatively stable phase with high values (>0.80), while similar or higher values for DI_1 are found within glacial MIS 4 & 6. The alkenone MAR record ranges between 30.9 and 0.3 mg m^{-2} yr^{-1}, although alkenone MARs generally do not exceed ~4 mg m^{-2} yr^{-1}. Observation of the alkenone MAR record (*fig. 8F*) clearly indicates increased accumulation rates during MIS 5 (~5 to 15 mg m^{-2} yr^{-1}), with a very distinct increase to 30.0 mg m^{-2} yr^{-1} just before MIS 5e.

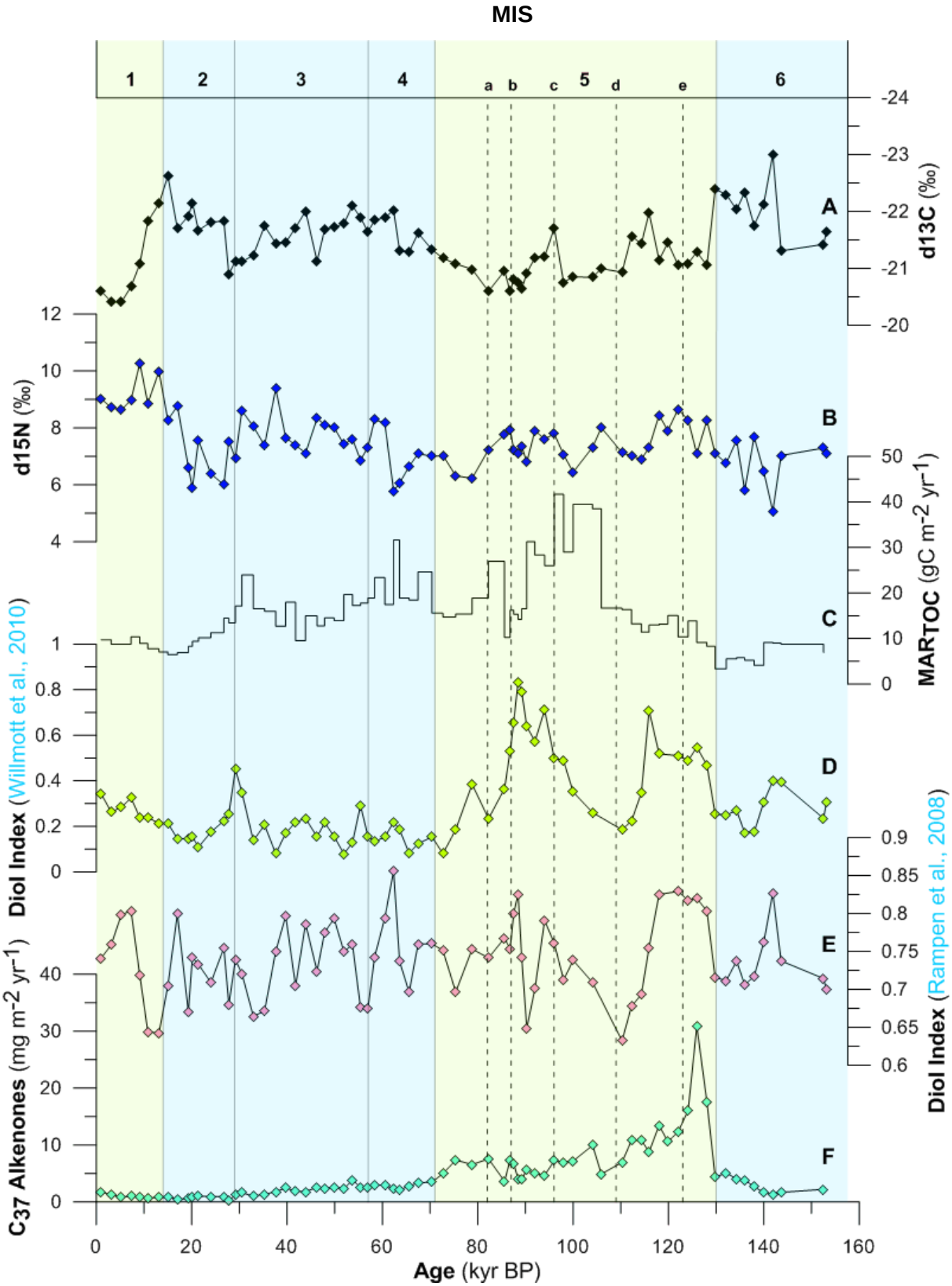

(Fig. 8) *Comparison of paleoproductivity records, plotted with geochemical records of ODP 1234. (**A**) $\delta^{13}C_{org}$. Note that the axis is reversed. (**B**) $\delta^{15}N$. (C) MAR of TOC. (**D**) Diol Index based on 1,14- en 1,13-diols. (**E**) Diol Index based on 1,14- & 1,15-diols. (**F**) MAR of $C_{37:2}$ and $C_{37:3}$ alkenones. MIS stages and substages (ages from Lisiecki & Raymo, 2005) are notified in the top of the figure. Background colors indicate interglacial (green) and glacial (blue) periods.*

4. Discussion

(4.1) Terrestrial input

The sediments recovered from ODP site 1234 have low abundances of brGDGTs, resulting in values below 0.05 for the BIT index (see *fig. 9c*). Such low values indicate a low input of river and soil derived tetraether lipids in the area off Concepción, during the last 150.000 years. The observed BIT values are remarkable low, taking into account the vicinity of considerable Andean river systems (see right side *fig. 1*, Río Bio-Bio and Río Itata; Muratli et al., 2010) in this area. It is evident that marine productivity at ODP site 1234 has overwhelmed terrestrial input during the last ~150 kyr. In contrast, higher BIT index values are found for sediments recovered from ODP site 1233 (located °5 further south than ODP site 1234, see *fig.1*). In the last ~25 kyr BP, BIT values as high as 0.13 are recorded for e.g. the Last Glacial Maximum (LGM; Verleye, 2011) despite the absence of large river systems in the vicinity of ODP Site 1233. ODP site 1234 is probably located to far from the major river estuaries to receive substantial amounts of river and soil derived tetraether lipids, which could have possibly resulted in the low observed abundances in the sediment core of ODP site 1234. Perhaps, shielding by a geological barrier or migrating discharge locations of Río Bio-Bio and/or Río Itata, could also have played a role during the last ~150 kyr. The $\delta^{13}C$ values were rather constant throughout the record (-23.0 to -20.4 ‰, see *fig. 8*) and correspond to those of marine organic matter (Meyers, 1994). This indicates that the TOC reflects mainly marine organic carbon and hardly any delivery of terrestrial organic carbon, as confirmed by the BIT index. Also, the relative abundance of C_{32} 1,15-diol (which may be produced by organisms that proliferate where major river systems discharge; De Bar et al., submitted) is quite low, since it makes up between ~9-20 % (data not shown) of the total 1,13- and 1,15 long-chain diol pool. This relative abundance is found to be substantially higher in surface sediments that have accumulated in the close proximity of a discharging river at the Atlantic Iberian margin (De Bar et al., submitted).

(4.2) Paleoenvironmental proxies

Below, the $U^{K'}_{37}$-, TEX^{H}_{86}-, and LDI-records derived from ODP site 1234 are compared with each other and with published data. Of the three different paleotemperature proxies assessed in this study, $U^{K'}_{37}$ SST estimations probably correlate best with mean annual SST (e.g. Lee et al., 2008), while the LDI and TEX_{86} probably correlate best with the warmest and coolest month, respectively (Lopes dos Santos., 2013). Also, the signals produced by the potential *Proboscia* paleoproductivity indicators (DI_1 and DI_2) and the more established haptophyte productivity indicator (total alkenone MAR) are discussed.

(4.2.1) $U^{K'}_{37}$

Comparison of the $U^{K'}_{37}$ SST record with published alkenone SST records nearby ODP site 1234, (Lamy et al., 2004; Kaiser et al., 2005, obtained from ODP site 1233 located °5 further south [see *fig.1*]; Kim et al., 2002, obtained at 33°S & 32°S on the Chilean continental slope) and Patagonian ice sheet (PIS) model simulations (Hunton et al., 2002), reveals that the $U^{K'}_{37}$ SST record (last ~70 kyr) from this study is in close agreement in terms of main tendencies and amplitudes. The few observed differences are well within calibration error. However, the resolution of the $U^{K'}_{37}$ SST record is too low to identify brief climatic events (e.g. Antarctic Cold Reversal [ACR]; 14-12.5 kyr BP; Jouzel et al., 1995) with certainty. SST fluctuations during the last glacial (~2-3 °C) observed in this study, seem to follow a similar pattern as observed in the Fe record (proxy for PIS extent) of ODP site 1233 (Lamy et al., 2004), confirming sensitivity of the PIS to SST changes as is observed in model simulation (Hunton et al., 2002).

The millennial scale SST fluctuation of the $U^{K'}_{37}$ SST record also may be related to Antarctic temperature changes (*fig. 9*), suggesting a direct link between SE Pacific SST changes and Antarctic climate fluctuations. However, there appears to be a substantial time lag between SE Pacific SSTs and changes in Antarctic climate of ~300-1200 kyr. Alkenone analysis at higher resolution is necessary to estimate the apparent lag more accurately, although the observed lag could also be an age model artefact. However, it has also been suggested that the coupling between oceanographic and Antarctic climatic changes has changed over time, due to an enhanced ACC (Pahnke et al., 2003).

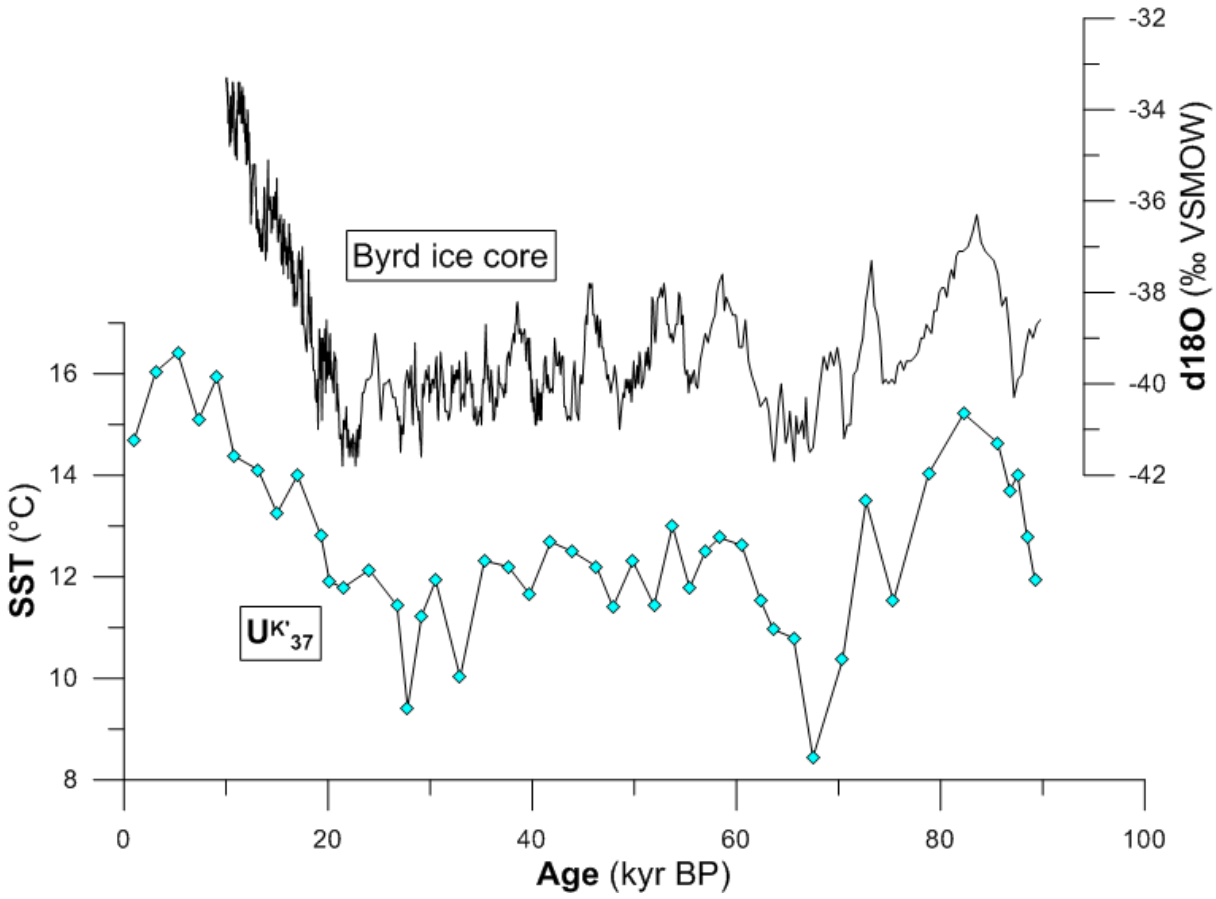

(Fig. 9) *Comparison of the $U^{K'}_{37}$ SST record from this study with the $\delta^{18}O$ record from the Byrd ice core (Johnsen et al., 1972) over the last 90 kyr. Age model of the Byrd ice core is synchronized to the GISP2 record via the fast variations of the global methane signal (Blunier & Brook, 2001). VSMOW = Vienna Standard Mean Ocean Water.*

(4.2.2) TEX_{86}

As described in section 3.2.3, the TEX^{H}_{86} SST record is characterized by abrupt single-point deviations from the underlying SST trend, which seem to reflect unrealistic paleotemperatures, assuming that no instrumental errors have occurred. These deviations do not seem to be present in the $U^{K'}_{37}$- and LDI SST records. Because BIT values for ODP site 1234 stay below 0.05, a terrestrial factor causing these deviations is highly unlikely. The cause for these abrupt deviations should perhaps be sought in the direction of *in situ* sedimentary production of GDGTs, affecting the TEX_{86} signature. At least two of the single-point (high-amplitude) interruptions show relative enhanced amounts of GDGT-1 and GDGT-2 (up to twice as much percentage wise, e.g. 18% instead of 9%) compared to other sediments.

Further research related to carbon isotope analysis of GDGTs and/or derivatives, could reveal if the TEX_{86} signal in the sediment core of ODP site 1234 is disturbed by *in situ* production of GDGTs. *In situ* production could perhaps be related to methane oxidizing Archaea, but if so, isolated GDGTs-1 & 2 and derivatives (i.e. biphytanes) should be relatively ^{13}C-depleted (i.e. more negative $\delta^{13}C$ values), since methane in sedimentary marine environments is usually ^{12}C-enriched. Therefore ^{13}C-depleted lipids could indicate that they emanate from GDGT-synthesizing organisms that carry out (anaerobic) methane oxidation. Studies already have unveiled high abundances of ^{13}C-depleted GDGTs-1 and 2 in cold methane seep sediments (e.g. Pancost et al., 2001) and have shown that ^{13}C-depleted GDGTs can be biosynthesized by methane oxidizing Archaea (e.g. Hinrichs et al., 1999). This way, exclusion of data points that are derived from sediments that induce a deviating TEX_{86} signal (likely due to methanogenic input), can be supported by (isotopic) evidence. However, application of the Methane Index (Zhang et al., 2011) did not generate extraordinary high values (<0.30), which indicates a normal marine environment for ODP site 1234, instead of a methane-rich environment due to e.g. the presence of gas-hydrates.

From the three SST proxies assessed in this study, the TEX_{86}^{H} temperature record most closely resembles the trend of the LR04 benthic $\delta^{18}O$ global stack during MIS 5, including the transient drop in SST during MIS 5e, which is not observed in the $U_{37}^{K'}$- and LDI SST records. Where the $U_{37}^{K'}$- and LDI SSTs increase until a maximum and subsequently decrease again, the TEX_{86}^{H} SST record peaks twice during MIS 5e within ~6 kyr. If the abrupt single-point deviations in the TEX_{86}^{H} SST record are ignored, estimated SSTs are generally lower compared with the $U_{37}^{K'}$- and LDI SST estimates. A reason that could cause deviations between the TEX_{86}^{H} SST record and the other two SST proxy records, is that the TEX_{86} reflects different water-depths of Thaumarchaeota, as is e.g. shown in the Benguela Upwelling System (Lee et al., 2008). In this study, GDGT analysis suggested a bias to colder SSTs, because the Thaumarchaeotal GDGT biosynthesis can allegedly take place below the mixed layer. The growing season of the biomarker source organisms could also be a factor that should be taken into account when evaluating SST proxy records. Although both the TEX_{86} and $U_{37}^{K'}$ seem to record annual mean SST, it has been shown that the growing season of the biomarker source organisms is different for haptophytes (Bac et al., 2003) and Thaumarchaeota (Wuchter et al., 2005) and proxy signals could therefore be biased to the preferred growing season of the source organism. However, according to Kaiser et al., 2015, the regional TEX_{86}^{H} calibration in the fjords and open ocean off Chile, has a statistically similar slope (but different intercept) as the global calibration based on suspended particulate

matter (Schouten et al., 2013), but their data could not reveal if seasonality played a role in the observed difference between the global calibration (Kim et al., 2010, 2012a,b) and the regional calibration off Chile.

Perhaps changes in upwelling intensity and related paleoproductivity could also explain some of the deviation and might have influenced the SST signals of both proxies. The largest peak in annual PP (and thus likely in haptophyte abundance) at the Chile margin occurs primarily during austral spring and summer, while Thaumarchaeota tend to be more abundant when PP is low (Wuchter et al., 2006). Therefore, GDGTs derived from Thaumarchaeota, could be biased to colder temperatures compared with alkenones derived from haptophytes. Thus the higher and more prolonged PP is during austral summer, the larger the cold temperature bias of Thaumarchaeotal GDGTs will be. Deviation between the $U^{K'}_{37}$- and TEX^{H}_{86} SST records, may be enhanced if the alkenones are biased towards spring and summer temperatures. Previous down core comparison between reconstructed SSTs of organic and inorganic proxies, confirms that the TEX^{H}_{86} SST estimates are probably related to austral winter month SSTs, at least in the region off Southeastern Australia (Lopes dos Santos., 2013). If the timing of peak annual PP has been during austral summer during the last ~150 kyr in the region off Concepción, this could possibly explain some of the observed deviation between the $U^{K'}_{37}$- and TEX^{H}_{86} SST records, e.g. during the Eemian interglacial, when haptophyte PP reaches its highest level of the last 150 kyr (see *fig. 8F*).

(4.2.3) LDI

Calculated diol fluxes were three orders of magnitude lower than alkenone- and GDGT fluxes. When comparing the LDI SST record with the $U^{K'}_{37}$- and TEX^{H}_{86} SST records, it should be noted that the LDI records larger temperature fluctuations and slightly higher temperatures in absolute terms. E.g. between MIS 5e to MIS 5d, the LDI SST decrease is larger than 8.3 °C, while it is 6.7 and 5.2 °C for the $U^{K'}_{37}$- and TEX^{H}_{86} SST records, respectively. Highest recorded SST during MIS 5e is 18.5 °C according to the LDI, while 17.8 and 14.6 °C are recorded according to the $U^{K'}_{37}$ and TEX_{86}, respectively. Deviation between the LDI- and TEX_{86} SST records appears to be largest.

The observed differences in absolute temperatures between the LDI SST record and the other two SST records in *fig. 9*, could be related to the possibility that the proxies record slightly different temperatures, e.g. because they are biased to different seasons or because the source organisms thrive at different depths. In addition, these factors can be affected by

changing climate conditions and source organisms could respond differently to these changes. According to Rampen et al. (2012), the LDI correlates best with late summer and early autumn SST on a global scale. This is confirmed by Lopes dos Santos et al. (2013) off the coast of SE Australia, where was found that SSTs as estimated by the LDI, seem to be related to austral summer SST, after comparison with seasonal SST estimates obtained from foraminiferal assemblages and modern SSTs. However, factors that could potentially lead to biases in the LDI SST estimates, still need to better constrained.

The LDI SST record contains two large outliers, especially the deviation at 62.4 kyr BP seems to be contrary in comparison with the $U^{K'}_{37}$- and the TEX^{H}_{86}-SST records. The large deviation at 90.3 kyr BP seems to be out of proportion with the other two records, but could coincide with the MIS 5b $\delta^{18}O$ minimum, which it would then slightly lead. Nevertheless, the LDI proxy seems to work well as a proxy for SST reconstruction in the upwelling region off Concepción, as it shows a similar general trend as the $U^{K'}_{37}$ and TEX^{H}_{86} records and because the LDI records known climatic events as indicated by $\delta^{18}O$ excursions.

(4.3) Regression analysis SST records

The $U^{K'}_{37}$- TEX^{H}_{86}- and LDI SST records have been cross-correlated with one another. Cross-correlation results and determinations are depicted in *fig. 10*.

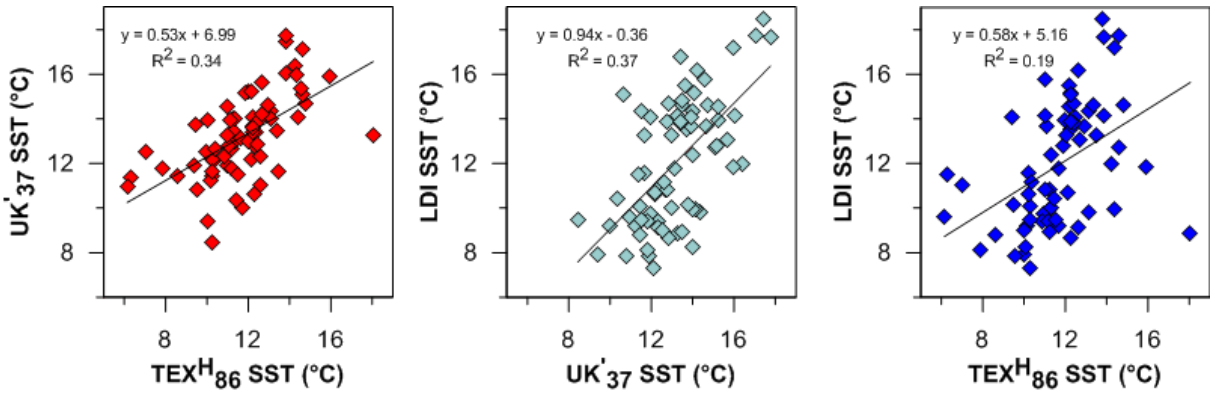

(Fig. 10) *Cross-correlation plots of the The $U^{K'}_{37}$- TEX^{H}_{86}- and LDI SST records. Black lines are regression lines that represent the best linear fit. Regression line formulas and coefficients of determination are denoted in the upper left corner of each plot.*

Regression analysis of the TEX^{H}_{86}- and the $U^{K'}_{37}$ SST records shows a statistically significant correlation (R^2 = 0.3445, n = 69, p < 0.0001). Statistically significant correlations are also found between the $U^{K'}_{37}$- and LDI SST records (R^2 = 0.3749, n = 72, p < 0.0001) as well as between the TEX^{H}_{86}- and LDI SST records (R^2 = 0.1918, n = 67, p = 0.0002).

If the two most extreme single-point deviations are excluded from the TEX_{86}^{H}data (related to relative enhanced amounts of GDGT-1 and GDGT-2, see section 4.3), the coefficient of determination (R^2) increases from 0.34 to 0.40 for the $U_{37}^{K'}$ & TEX_{86}^{H} correlation and from 0.19 to 0.30 for the LDI & TEX_{86}^{H} correlation. As shown by the R^2 values, the correlations between the SST records are not very strong. However, the differences between e.g. the TEX_{86}^{H}- and the LDI data (which appear to be largest, see section 4.4), are not significant (at the 5% significance level, based on a two-tailed t-Test; p = 0.4614)

(4.4) Paleoproductivity

In this section, the paleoproductivity at ODP Site 1234 is discussed, by assessing sedimentary nitrogen isotopes and evaluating the results as indicated by the diol indices of Rampen et al. (2008) and Willmott et al. (2010).

(4.4.1) Stable nitrogen isotopes

Upwelling areas and are not only associated with relatively high PP, but are also characterized by OMZs, which originate due to oxygen demand required for the decay of settling particulate organic matter. In layers of the water column with absence or low amounts of oxygen, bacterial reduction of nitrate (denitrification) takes place, characterized by large isotopic fractionation, significantly enriching the residual nitrate pool of the upwelling water in ^{15}N. Therefore, variation in the signature of denitrification (residual ^{15}N-enriched NO_3^- assimilated by phytoplankton and converted to organic N), as delivered by the sedimentation of organic matter, is often reflected by $\delta^{15}N$ values of TOC (Martinez et al., 2006). The stable nitrogen isotopic ratios of sediment can therefore be analysed to assess the degree of denitrification (e.g. Altabet & Francois, 1994), which in turn could indicate the size of the OMZ and associated PP. Nitrogen stable isotopes in organic carbon often show a globally similar pattern throughout the last 60 kyr, with heavier $\delta^{15}N$ values in MIS 1 and 2 and lower values in MIS 2, 3 and 4 (e.g. Galbraith et al., 2004). Along the Chilean continental margin, numerous sediment studies have been conducted, which have revealed changes in marine sub-surface conditions in the HCS on a glacial-interglacial time-scale. During deglaciation, interpreted changes include: a major reorganization of the OMZ and an increase in water column denitrification, represented by high interglacial sedimentary $\delta^{15}N$ values (Altabet, 2006; Robinson et al., 2007). The deglacial increase in denitrification seems to have been decoupled from local PP and in some regions and instead triggered by fresh-water pulses from a melting PIS (De Pol-Holz et al., 2006).

Surprisingly, increased interglacial $\delta^{15}N$ values are not observed in the $\delta^{15}N$ record obtained from ODP site 1234. The $\delta^{15}N$ values in the sediment core of ODP site 1234 were relatively low (5.9-10.3 ‰) compared with the record of Martinez et al. (2006) (~9-13 ‰) that covers the last 50 kyr at ODP site 1233 (located °5 further south). However, there is a resemblance in trends with the record from Martinez et al. (2006), e.g. a $\delta^{15}N$ increase that initiates at the beginning of Termination I (18-11 kyr BP; Denton et al., 2010) and a decrease in $\delta^{15}N$ values during the early Holocene. Although an increase in $\delta^{15}N$ at ODP site 1234 is observed over Termination I, the $\delta^{15}N$ values representing the last interglacial (MIS 5) are similar or lower than that of the last glacial. Perhaps, just as De Pol-Holz et al. (2006) have proposed for the area off northern Chile, denitrification is also decoupled from PP in the area off Concepción, regarding the peaks of relatively high productivity and relatively low $\delta^{15}N$ values during MIS 5 (*fig. 8*). Unfortunately, the resolution of this study is too low to confirm a millennial scale oscillation in $\delta^{15}N$ values. Further research focusing on $\delta^{15}N$ analysis at higher resolution could possibly reveal an Antarctic forcing/timing, as is proposed by Martinez et al. (2006).

(4.4.2) Diol Indices

Recently, the occurrence of 1,14-diols has also been reported in cultures of the microalgae *Apedinella Radians* of the heterokont genus (Rampen et al., 2011). According to Rampen et al. (2011), *A. Radians* biosynthesizes C_{28}, C_{30} and C_{32} 1,14-diols, of which the last mentioned is not produced by *Proboscia* diatoms. In contrast, *Proboscia* produces the mono-unsaturated $C_{28:1}$ and $C_{30:1}$ 1,14-diols, which are not produced by *A. Radians*. Moreover, a typical biomarker for *Proboscia* is the C_{29} 12-OH fatty acid (Sinninghe Damsté et al., 2003). Since the C_{32} 1,14-diol is not detected during lipid analysis, in contrast to the $C_{30:1}$ 1,14 diol as well as the C_{29} 12-OH fatty acid, it is highly likely that *Proboscia* is the source of the 1,14-diols detected in the sediments. Absence of the C_{32} 1,14-diol suggests that the productivity proxies based on 1,14-diols are probably not compromised by *A. Radians* 1,14-diol production at ODP site 1234.

As can be observed in *fig. 9* and is reported in section 3.2.5, the three assessed paleoproductivity proxies (DI_1, DI_2 and alkenone MAR) generate distinctly different trends. DI2 seems to indicate a very different *Proboscia* productivity signal compared to DI1, despite the indications that 1,13- and 1,15-diols are likely produced by the same class of algae (Eustigmatophyceae; e.g. Volkman et al., 1999; Méjanelle et al., 2003). Apart from the uncertainty that is related to the source of 1,13- and 1,15-diols, the DI_1 was originally used as a proxy that could indicate past upwelling intensities in the Arabian Sea and has shown that

the upwelling intensity in the Arabian Sea has a strong relation with global climate (Rampen et al., 2008). A similar strong inverse relationship of the DI_1 with the LR04 benthic $\delta^{18}O$ stack (Lisickie & Raymo, 2005) is not observed in this study. This implies that the upwelling intensity in the area off Concepción is not directly linked to global climate and probably primarily forced by a different mechanism. It has already been shown that the DI_1 is affected by temperature (Rampen et al., 2014) and therefore not suitable as a global applicable paleoproductivity proxy. The C_{30} 1,15-diol makes up about ~15-46 % of the total long-chain diol pool in the sediments from ODP site 1234, which is mostly a larger contribution to the total long-chain diol pool than the amount of C_{28} or C_{30} 1,13-diols (~4-22 % and ~9-33%, respectively). Although all three diols are part of LDI and contribute substantially to the total long-chain diol pool, the C_{30} 1,15-diol production probably has a stronger relation with SST than the C_{28} and C_{30} 1,13-diol production (Rampen et al., 2012). Since there have been large temperature variations throughout the last ~150 kyr in the Southeast Pacific (as indicated by the results in *fig. 7*) and the DI_1 is partly based on the C_{30} 1,15-diol, the SST variation likely affects the *Proboscia* productivity signal that is indicated by the DI_1.

Additionally, the relationship of the diol biosynthesizing organism with upwelling, might differ between regions and could therefore compromise the diol indices. When applying the diol indices, the local relation of *Proboscia* diatoms with upwelling conditions, should always be taken into account. This is likely different per location, depending on the competition within the local ecosystem and the relation of different *Proboscia* species to specific environmental factors (Rampen et al., 2014). However, DI_2 seems to provide a better pronounced signal with respect to glacial/interglacial periods than DI1 does, making DI_2 a better suitable proxy for reconstructing *Proboscia* paleoproductivity in the area off Concepción and is thus further evaluated in this study.

In *fig. 11*, the 1,13- and 1,14-diol accumulation rates are plotted, to investigate what causes the maxima in the DI_2. The 1,13- and 1,14-diol accumulation rates are also compared with TOC and alkenone accumulation rates, in order to clarify if changes in the DI_2 can be attributed to increased organic matter accumulation and to see how haptophyte productivity compares with *Proboscia* productivity.

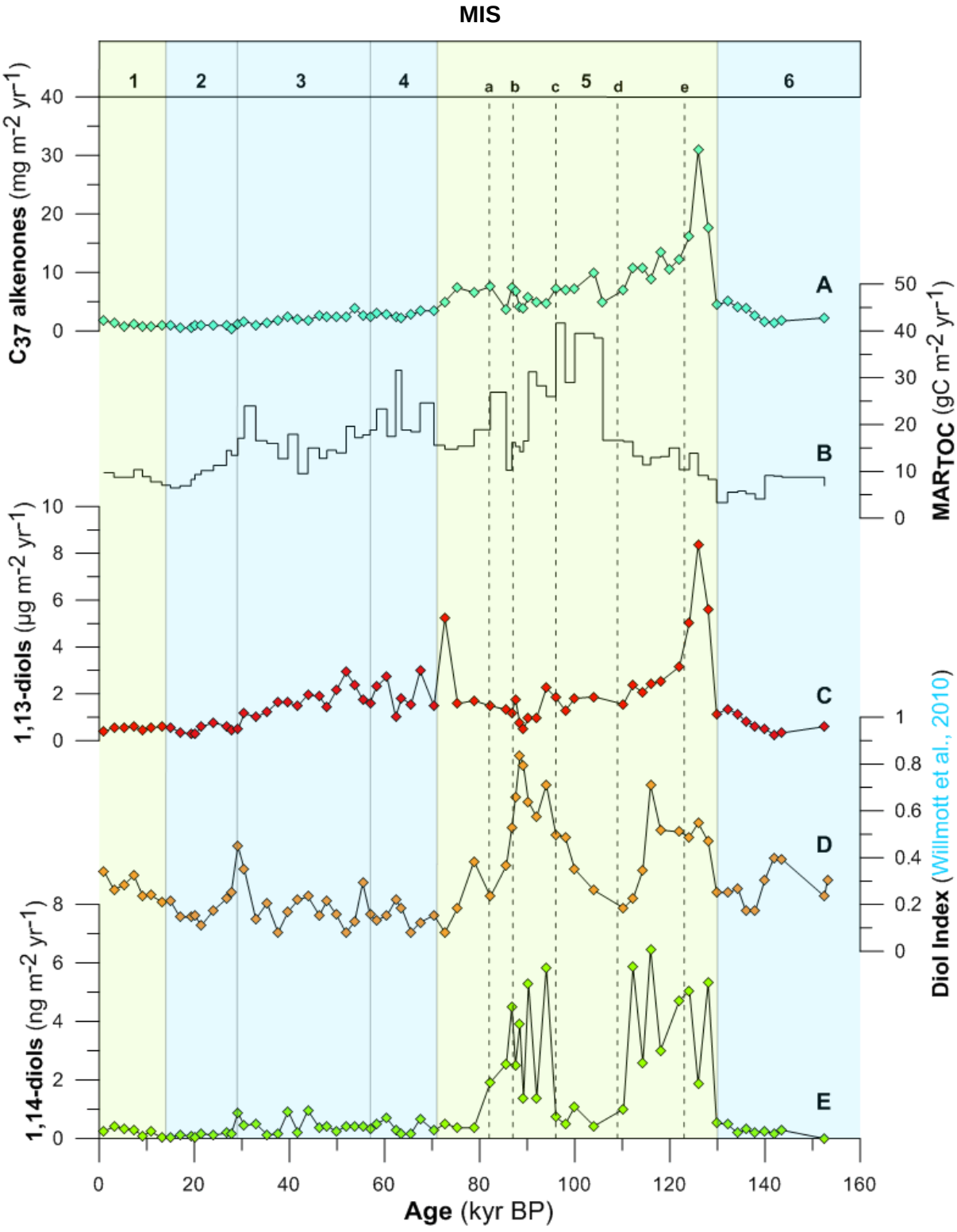

(Fig. 11) *Diol Index, 1,13-diol MAR and 1,14-diol MAR compared with MAR_{TOC} and C_{37} alkenone MAR. (**A**) MAR of $C_{37:2}$ and $C_{37:3}$ alkenones. (**B**) MAR of TOC. (**C**) MAR of C_{28} + C_{30} 1,13-diols. (**D**) Diol Index (Willmott et al., 2010). (**E**) MAR of C_{28} + C_{30} 1,14-diols. MIS stages and substages (ages from Lisiecki & Raymo, 2005) are notified in the top of the figure. Background colors indicate interglacial (green) and glacial (blue) periods.*

The proxy records for haptophyte productivity (*fig. 11A*) and *Proboscia* productivity (*fig. 11D*) do not correlate with one another according to findings of this study. While haptophyte productivity clearly peaks during MIS 5e, *Proboscia* productivity peaks twice during MIS 5 and seems to sustain at a higher level for longer periods. Fluctuations during the last 75 kyr in the DI_2 record, seem to be caused by fluctuations in the 1,13-diol concentration (*fig 11C*), since the concentration of 1,14-diols remains relatively constant throughout this period. This is different for MIS 5, in which the relative importance of *Proboscia* diatoms seems to be high between 98.0-86.8 and 128.1-115.9 kyr BP, as indicated by the C_{28} and C_{30} 1,14-diol MAR (*fig 11E*). These peaks represent high *Proboscia* productivity and correspond to peaks in the DI_2 (*fig. 11D*). This suggests that the source organism producing the 1,13-diols and the *Proboscia* diatoms do not respond similarly to environmental changes in the area off Concepción.

Of the two evident *Proboscia* productivity peaks indicated by the DI_2, only the maximum that occurs during MIS 5e (128.1-115.9) is observed in the Proboscia diatom biomarker (C_{28} 1,14-diol) record of Contreras et al. (2010), which is obtained off the Peruvian coast at ODP site 1229 (located approximately 25.5° further north than ODP site 1234). The peak observed between 98.0-86.8 kyr BP in this study, is not observed in the Proboscia diatom biomarker record from ODP site 1229. In the equatorial Pacific Ocean, high SSTs generally induce a more stable water column, enhancing stratification and reducing upwelling (Chavez et al., 1999). Therefore, Contreras et al. (2010) proposed that high abundances of *Proboscia* diatom biomarkers are indicative of enhanced water column stratification, based on a high correlation between SST and a *Proboscia* biomarker found in their study. This high correlation between SST and the C_{28} 1,14-diol is not observed in this study (data not shown). In fact, C_{28} 1,14-diols have been higher during the last glacial than during the current interglacial (data not shown), contradicting the hypothesis of Contreras et al. (2010).

If the hypothesis of Contreras et al. (2010) is valid, perhaps SSTs were not high enough between 98.0-86.8 kyr BP at ODP site 1229, to cause enhanced water column stratification and subsequent *Proboscia* diatom proliferation. It would be remarkable if SSTs at Peruvian margin (13.5°S) were lower than at the central-south Chilean margin (ODP site 1234; 36°S), but could theoretically be explained by differences in upwelling intensity between the two areas, halfway MIS 5. Perhaps, upwelling intensity and thus the supply of cold nutrient-rich waters in the area off central Peru, was high enough to sufficiently cool surface waters and thus prevent water column stratification. At the same time, in the area off Concepción, upwelling intensity could be low enough to allow higher SSTs and subsequent stratification, providing optimal conditions for *Proboscia* diatoms to proliferate. Different studies have

shown that productivity rates can be different along the western South-American coast during the same time interval, e.g. due to different wind regimes at different latitudes. E.g. Mohtadi et al. (2008) have found higher interglacial and Holocene paleoproductivities for the central-south Chilean margin and have linked this to the onset of active upwelling and increased export production. This in contrast with north-central Chile, where higher paleoproductivity is interpreted for the LGM (Mohtadi & Hebbeln, 2004). In the region off Concepción (central-south Chilean margin), paleoproductivity was probably reduced during the LGM, due to direct onshore-blowing winds that prevented upwelling, because the Southern Westerlies were likely located further north (Mohtadi et al., 2008). Besides upwelling intensity and water column stratification, there are also other factors that probably have influenced PP off the western South-American coast. During the last 100.000 years, PP along the Chilean margin has probably varied on a precessional scale (~20 kyr) and may be influenced by glacial-interglacial variability in iron supply from the continent, due to changes in precipitation (Montecino & Lange, 2009). Hutchins et al. (2002) have shown that iron limitation is presently a major constraint on general PP along the eastern South Pacific coast. Perhaps, these findings should be interpreted as evidence for iron control on past productivity in this region. Bulk sediment analysis conducted by Lamy et al. (2004), has already shown that changing Fe contents have been found in the sediment core from ODP site 1233, due to glacial erosion processes that enhanced the glaciofluvial input of Fe. However, further research (i.e. aeolian dust input reconstruction) is required to provide more evidence for this hypothesis.

5. Conclusion

A multiproxy approach to reconstruct past SSTs, has led to the conclusion that the LDI can be considered as a suitable proxy to reconstruct SSTs for the area off Concepción over the last ~150 kyr. The location of ODP site 1234 in an upwelling system, does not seem to disturb the SST signal. This is indicated by the close agreement of three independent organic temperature proxies over glacial-interglacial time scales. The $U_{37}^{K'}$-, TEX_{86}^{H}- and LDI SST records obtained from ODP site 1234, agree in terms of main tendencies and amplitudes, both between the different paleotemperature proxies and compared with published records. Alongside the coherent pattern between the SST records, the TEX_{86}^{H} SST record generally indicates colder SSTs than the $U_{37}^{K'}$ and LDI. Of the three assessed SST proxies, the $U_{37}^{K'}$ SST record seems to most closely resemble glacial/interglacial temperatures, as indicated by the $\delta^{18}O$ excursions (slow glacial build-up and rapid deglaciation) of the LR04 benthic global stack. Both the TEX_{86}^{H}- and LDI SST records also closely resemble these $\delta^{18}O$ excursions, but seem to have some abrupt single-point deviations, interrupting the general SST trend.

The single-point deviations leading to exceptionally high temperatures in the TEX_{86}^{H} SST record, might be caused by *in situ* production of GDGT-1 and GDGT-2 of anaerobic methanotrophs, disturbing the TEX_{86} signal. Marine productivity has probably overwhelmed terrestrial input at ODP site 1234 over the last ~150 kyr, as indicated by low BIT values (≤ 0.05) and relatively low abundance of the C_{32} 1,15-diol. Therefore it remains uncertain if fluvially transported terrestrial organic matter can disturb the paleoproductivity signals of the different diol proxies.

Paleoproductivity assessment on basis of biomarkers from haptophyte algae and Proboscia diatoms, revealed different productivity signals for the last ~150 kyr. While the DI_1 is unsuitable as a proxy for Proboscia productivity in the area off Concepción, the DI_2 and C_{37} alkenone MAR seem to detect substantial changes in past productivity. The C_{37} alkenone MAR indicates structural higher haptophyte paleoproductivity during MIS 5 and a strong productivity peak just before the MIS 5e peak. The DI_2 indicates two periods of increased *Proboscia* diatom productivity during the last interglacial, namely during MIS 5b & 5c and for the Eemian interglacial (MIS 5e). The differences in 1,13- and 1,14-diol concentration that affect the DI_2 signal do not seem to occur simultaneously. This suggests that the source organism producing the 1,13-diols and the *Proboscia* diatoms are not regulated by the same forcing. There is no correlation found between SSTs and 1,14-diol concentration in this study, indicating that the diol indices are not reflecting enhanced water column stratification in the area off Concepción. Further research at higher resolution (e.g. on a [sub]millennial time scale) needs to be conducted, to constrain the lag between SSTs and Antarctic climate, more precise identification of climatic events and/or millennial oscillation in stable nitrogen isotopes, as indicated by published records with higher resolution.

References

Altabet, M. A., & Francois, R. (1994). Sedimentary nitrogen isotopic ratio as a recorder for surface ocean nitrate utilization. *Global biogeochemical cycles*, *8*(1), 103-116.

Altabet, M. A. (2006). Constraints on oceanic N balance/imbalance from sedimentary 15 N records. *Biogeosciences Discussions*, *3*(4), 1121-1155.

Bac, M. G., Buck, K. R., Chavez, F. P., & Brassell, S. C. (2003). Seasonal variation in alkenones, bulk suspended POM, plankton and temperature in Monterey Bay, California: implications for carbon cycling and climate assessment. *Organic geochemistry*, *34*(6), 837-855.

Blunier, T., & Brook, E. J. (2001). Timing of millennial-scale climate change in Antarctica and Greenland during the last glacial period. *Science*, *291*(5501), 109-112.

Brassell, S. C. (1993). Applications of biomarkers for delineating marine paleoclimatic fluctuations during the Pleistocene. In *Organic Geochemistry*(pp. 699-738). Springer US.

Chavez, F. P., Strutton, P. G., Friederich, G. E., Feely, R. A., Feldman, G. C., Foley, D. G., & McPhaden, M. J. (1999). Biological and chemical response of the equatorial Pacific Ocean to the 1997-98 El Niño. *Science*, *286*(5447), 2126-2131.

Chavez, F. P., Ryan, J., Lluch-Cota, S. E., & Ñiquen, M. (2003). From anchovies to sardines and back: multidecadal change in the Pacific. *Ocean science*, *299*(5604), 217-221.

Contreras, S., Lange, C. B., Pantoja, S., Lavik, G., Rincón-Martínez, D., & Kuypers, M. M. (2010). A rainy northern Atacama Desert during the last interglacial. *Geophysical Research Letters*, *37*(23).

Dahl-Jensen, D., Albert, M. R., Aldahan, A., Azuma, N., Balslev-Clausen, D., Baumgartner, M., ... & Bourgeois, J. C. (2013). Eemian interglacial reconstructed from a Greenland folded ice core. *Nature*, *493*(7433), 489-494.

De Jonge, C., Hopmans, E. C., Stadnitskaia, A., Rijpstra, W. I. C., Hofland, R., Tegelaar, E., & Damsté, J. S. S. (2013). Identification of novel penta-and hexamethylated branched glycerol dialkyl glycerol tetraethers in peat using HPLC–MS 2, GC–MS and GC–SMB-MS. *Organic geochemistry*, *54*, 78-82.

De Leeuw, J. W., Irene, W., Rijpstra, C., & Schenck, P. A. (1981). The occurrence and identification of C 30, C 31 and C 32 alkan-1, 15-diols and alkan-15-one-1-ols in Unit I and Unit II Black Sea sediments. *Geochimica et Cosmochimica Acta*, *45*(11), 2281-2285.

De Pol-Holz, D., Ulloa, O., Dezileau, L., Kaiser, J., Lamy, F., & Hebbeln, D. (2006). Melting of the Patagonian Ice Sheet and deglacial perturbations of the nitrogen cycle in the eastern South Pacific. *Geophysical Research Letters*, *33*(4).

Denton, G. H., Anderson, R. F., Toggweiler, J. R., Edwards, R. L., Schaefer, J. M., & Putnam, A. E. (2010). The last glacial termination. *Science*,*328* (5986), 1652-1656.

Escribano, R., Daneri, G., Farías, L., Gallardo, V. A., González, H. E., Gutiérrez, D., ... & Braun, M. (2004). Biological and chemical consequences of the 1997–1998 El Niño in the Chilean coastal upwelling system: a synthesis. *Deep Sea Research Part II: Topical Studies in Oceanography*, *51*(20), 2389-2411.

Fernández, E., & Bode, A. (1994). Succession of phytoplankton assemblages in relation to the hydrography in the southern Bay of Biscay: a multivariate approach. *Scientia Marina, 58*(3), 191-205.

Galbraith, E. D., Kienast, M., Pedersen, T. F., & Calvert, S. E. (2004). Glacial-interglacial modulation of the marine nitrogen cycle by high-latitude O2 supply to the global thermocline. *Paleoceanography, 19*(4).

Ganeshram, R. S., & Pedersen, T. F. (1998). Glacial-interglacial variability in upwelling and bioproductivity off NW Mexico: Implications for quaternary paleoclimate. *Paleoceanography*, *13*(6), 634-645.

Herrera, L., & Escribano, R. (2006). Factors structuring the phytoplankton community in the upwelling site off El Loa River in northern Chile. *Journal of Marine Systems*, *61*(1), 13-38.

Heusser, L., Heusser, C., Mix, A., & McManus, J. (2006). Chilean and Southeast Pacific paleoclimate variations during the last glacial cycle: directly correlated pollen and δ 18 O records from ODP Site 1234. *Quaternary Science Reviews*, *25*(23), 3404-3415.

Hinrichs, K. U., Hayes, J. M., Sylva, S. P., Brewer, P. G., & DeLong, E. F. (1999). Methane-consuming archaebacteria in marine sediments. *Nature*, *398*(6730), 802-805.

Hopmans, E. C., Weijers, J. W., Schefuß, E., Herfort, L., Damsté, J. S. S., & Schouten, S. (2004). A novel proxy for terrestrial organic matter in sediments based on branched and isoprenoid tetraether lipids. *Earth and Planetary Science Letters*, *224*(1), 107-116.

Hopmans, E. C., Schouten, S., & Damsté, J. S. S. (2016). The effect of improved chromatography on GDGT-based palaeoproxies. *Organic Geochemistry, 93*, 1-6.

Huguet, C., Hopmans, E. C., Febo-Ayala, W., Thompson, D. H., Damsté, J. S. S., & Schouten, S. (2006). An improved method to determine the absolute abundance of glycerol dibiphytanyl glycerol tetraether lipids. *Organic Geochemistry*, *37*(9), 1036-1041.

Hutchins, D. A., Hare, C. E., Weaver, R. S., Zhang, Y., Firme, G. F., DiTullio, G. R., ... & Trick, C. G. (2002). Phytoplankton iron limitation in the Humboldt Current and Peru Upwelling. *Limnology and Oceanography*, *47*(4), 997-1011.

Johnsen, S. J., Dansgaard, W., Clausen, H. B., & Langway, C. C. (1972). Oxygen isotope profiles through the Antarctic and Greenland ice sheets. *Nature*, *235*(5339), 429-434.

Jouzel, J., Vaikmae, R., Petit, J. R., Martin, M., Duclos, Y., Stievenard, M., ... & Barkov, N. I. (1995). The two-step shape and timing of the last deglaciation in Antarctica. *Climate Dynamics*, *11*(3), 151-161.

Kaiser, J., Lamy, F., & Hebbeln, D. (2005). A 70-kyr sea surface temperature record off southern Chile (Ocean Drilling Program Site 1233). *Paleoceanography, 20*(4).

Kaiser, J., Schouten, S., Kilian, R., Arz, H. W., Lamy, F., & Damsté, J. S. S. (2015). Isoprenoid and branched GDGT-based proxies for surface sediments from marine, fjord and lake environments in Chile. *Organic Geochemistry, 89-90*, 117-127.

Kim, J. H., Schneider, R. R., Hebbeln, D., Müller, P. J., & Wefer, G. (2002). Last deglacial sea-surface temperature evolution in the Southeast Pacific compared to climate changes on the South American continent. *Quaternary Science Reviews, 21*(18), 2085-2097.

Kim, J. H., Van der Meer, J., Schouten, S., Helmke, P., Willmott, V., Sangiorgi, F., ... & Damsté, J. S. S. (2010). New indices and calibrations derived from the distribution of crenarchaeal isoprenoid tetraether lipids: Implications for past sea surface temperature reconstructions. *Geochimica et Cosmochimica Acta, 74*(16), 4639-4654.

Kim, J. H., Crosta, X., Willmott, V., Renssen, H., Bonnin, J., Helmke, P., ... & Sinninghe Damsté, J. S. (2012a). Holocene subsurface temperature variability in the eastern Antarctic continental margin. *Geophysical Research Letters, 39*(6).

Kim, J. H., Romero, O. E., Lohmann, G., Donner, B., Laepple, T., Haam, E., & Damste, J. S. S. (2012b). Pronounced subsurface cooling of North Atlantic waters off Northwest Africa during Dansgaard–Oeschger interstadials. *Earth and Planetary Science Letters, 339*, 95-102.

Koning, E., Van Iperen, J. M., Van Raaphorst, W., Helder, W., Brummer, G. J., & Van Weering, T. C. E. (2001). Selective preservation of upwelling-indicating diatoms in sediments off Somalia, NW Indian Ocean. *Deep Sea Research Part I: Oceanographic Research Papers, 48*(11), 2473-2495.

Lee, K. E., Kim, J. H., Wilke, I., Helmke, P., & Schouten, S. (2008). A study of the alkenone, TEX86, and planktonic foraminifera in the Benguela Upwelling System: Implications for past sea surface temperature estimates. *Geochemistry, Geophysics, Geosystems, 9*(10).

Lamy, F., Rühlemann, C., Hebbeln, D., & Wefer, G. (2002). High-and low-latitude climate control on the position of the southern Peru-Chile Current during the Holocene. *Paleoceanography, 17*(2).

Lamy, F., Kaiser, J., Ninnemann, U., Hebbeln, D., Arz, H. W., & Stoner, J. (2004). Antarctic timing of surface water changes off Chile and Patagonian ice sheet response. *Science, 304*(5679), 1959-1962.

Lisiecki, L. E., & Raymo, M. E. (2005). A Pliocene-Pleistocene stack of 57 globally distributed benthic δ18O records. *Paleoceanography, 20*(1).

Liu, X. L., Lipp, J. S., Simpson, J. H., Lin, Y. S., Summons, R. E., & Hinrichs, K. U. (2012). Mono-and dihydroxyl glycerol dibiphytanyl glycerol tetraethers in marine sediments: identification of both core and intact polar lipid forms. *Geochimica et Cosmochimica Acta*, *89*, 102-115.

Lopes dos Santos, R. A., Spooner, M. I., Barrows, T. T., De Deckker, P., Sinninghe Damsté, J. S., & Schouten, S. (2013). Comparison of organic (UK'37, TEXH86, LDI) and faunal proxies (foraminiferal assemblages) for reconstruction of late Quaternary sea surface temperature variability from offshore southeastern Australia. *Paleoceanography*, *28*(3), 377-387.

Martin, M. W., Kato, T. T., Rodriguez, C., Godoy, E., Duhart, P., McDonough, M., & Campos, A. (1999). Evolution of the late Paleozoic accretionary complex and overlying forearc-magmatic arc, south central Chile (38°–41° S): Constraints for the tectonic setting along the southwestern margin of Gondwana. *Tectonics*, *18*(4), 582-605.

Martinez, P., Lamy, F., Robinson, R. R., Pichevin, L., & Billy, I. (2006). Atypical δ 15 N variations at the southern boundary of the East Pacific oxygen minimum zone over the last 50ka. *Quaternary Science Reviews*,*25*(21), 3017-3028.

McDonald, G. R., Hudson, A. L., Dunn, S. M., You, H., Baker, G. B., Whittal, R. M., ... & Holt, A. (2008). Bioactive contaminants leach from disposable laboratory plasticware. *Science*, *322*(5903), 917-917.

Méjanelle, L., Sanchez-Gargallo, A., Bentaleb, I., & Grimalt, J. O. (2003). Long chain n-alkyl diols, hydroxy ketones and sterols in a marine eustigmatophyte, Nannochloropsis gaditana, and in Brachionus plicatilis feeding on the algae. *Organic Geochemistry*, *34*(4), 527-538.

Meyers, P. A. (1994). Preservation of elemental and isotopic source identification of sedimentary organic matter. *Chemical Geology*, *114*(3-4), 289-302.

Mix, A.C., Tiedemann, R., Blum, P., et al., 2003. *Proc. ODP, Init. Repts.,* 202: College Station, TX (Ocean Drilling Program).

Mohtadi, M., & Hebbeln, D. (2004). Mechanisms and variations of the paleoproductivity off northern Chile (24 S–33 S) during the last 40,000 years. *Paleoceanography*, *19*(2).

Mohtadi, M., Rossel, P., Lange, C. B., Pantoja, S., Böning, P., Repeta, D. J., ... & Brumsack, H. J. (2008). Deglacial pattern of circulation and marine productivity in the upwelling region off central-south Chile. *Earth and Planetary Science Letters*, *272*(1), 221-230.

Montecino, V., Paredes, M. A., Paolini, P., & Rutllant, J. (2006). Revisiting chlorophyll data along the coast in north-central Chile, considering multiscale environmental variability. *Rev. Chil. Hist. Nat*, *79*, 213-223.

Montecino, V., & Lange, C. B. (2009). The Humboldt Current System: Ecosystem components and processes, fisheries, and sediment studies. *Progress in Oceanography*, *83*(1), 65-79.

Müller, P. J., Kirst, G., Ruhland, G., Von Storch, I., & Rosell-Melé, A. (1998). Calibration of the alkenone paleotemperature index U 37 K′ based on core-tops from the eastern South Atlantic and the global ocean (60 N-60 S). *Geochimica et Cosmochimica Acta*, *62*(10), 1757-1772.

Muratli, J. M., Chase, Z., McManus, J., & Mix, A. (2010). Ice-sheet control of continental erosion in central and southern Chile (36–41 S) over the last 30,000 years. *Quaternary Science Reviews*, *29*(23), 3230-3239.

Neelin, J. D., Battisti, D. S., Hirst, A. C., Jin, F. F., Wakata, Y., Yamagata, T., & Zebiak, S. E. (1998). ENSO theory. *Journal of Geophysical Research: Oceans*, *103*(C7), 14261-14290.

Ocean Climate Laboratory, World Ocean Atlas 1998, 1999. National Oceanographic Data Center, Silver Spring, MD, p. 16.

Pancost, R. D., Hopmans, E. C., & Damsté, J. S., Medinaut Shipboard Scientific Party (2001). Archaeal lipids in Mediterranean cold seeps: molecular proxies for anaerobic methane oxidation. *Geochimica et Cosmochimica Acta*, *65*(10), 1611-1627.

Pahnke, K., Zahn, R., Elderfield, H., & Schulz, M. (2003). 340,000-year centennial-scale marine record of Southern Hemisphere climatic oscillation. *Science*, *301*(5635), 948-952.

Plancq, J., Grossi, V., Pittet, B., Huguet, C., Rosell-Melé, A., & Mattioli, E. (2015). Multi-proxy constraints on sapropel formation during the late Pliocene of central Mediterranean (southwest Sicily). *Earth and Planetary Science Letters*, *420*, 30-44.

Prahl, F. G., & Wakeham, S. G. (1987). Calibration of unsaturation patterns in long-chain ketone compositions for palaeotemperature assessment. *Nature, 330*, 367–369

Prahl, F. G., Muehlhausen, L. A., & Zahnle, D. L. (1988). Further evaluation of long-chain alkenones as indicators of paleoceanographic conditions.*Geochimica et Cosmochimica Acta*, *52*(9), 2303-2310.

Rampen, S. W., Schouten, S., Wakeham, S. G., & Damsté, J. S. S. (2007). Seasonal and spatial variation in the sources and fluxes of long chain diols and mid-chain hydroxy methyl alkanoates in the Arabian Sea. *Organic Geochemistry*, *38*(2), 165-179.

Rampen, S. W., Schouten, S., Koning, E., Brummer, G. J. A., & Damsté, J. S. S. (2008). A 90 kyr upwelling record from the northwestern Indian Ocean using a novel long-chain diol index. *Earth and Planetary Science Letters*, *276*(1), 207-213.

Rampen, S. W., Schouten, S., Schefuß, E., & Damsté, J. S. S. (2009). Impact of temperature on long chain diol and mid-chain hydroxy methyl alkanoate composition in Proboscia diatoms: results from culture and field studies. *Organic Geochemistry*, *40*(11), 1124-1131.

Rampen, S. W., Schouten, S., & Damsté, J. S. S. (2011). Occurrence of long chain 1, 14-diols in Apedinella radians. *Organic geochemistry*, *42*(5), 572-574.

Rampen, S. W., Willmott, V., Kim, J. H., Uliana, E., Mollenhauer, G., Schefuß, E., ... & Schouten, S. (2012). Long chain 1, 13-and 1, 15-diols as a potential proxy for palaeotemperature reconstruction. *Geochimica et Cosmochimica Acta*, *84*, 204-216.

Rampen, S. W., Willmott, V., Kim, J. H., Rodrigo-Gámiz, M., Uliana, E., Mollenhauer, G., ... & Schouten, S. (2014). Evaluation of long chain 1, 14-alkyl diols in marine sediments as indicators for upwelling and temperature. *Organic Geochemistry*, *76*, 39-47.

Ramos, M., Dewitte, B., Pizarro, O., & Garric, G. (2008). Vertical propagation of extratropical Rossby waves during the 1997–1998 El Niño off the west coast of South America in a medium-resolution OGCM simulation. *Journal of Geophysical Research: Oceans*, *113*(C8).

Repeta, D. J. (1989). Carotenoid diagenesis in recent marine sediments: II. Degradation of fucoxanthin to loliolide. *Geochimica et Cosmochimica Acta*, *53*(3), 699-707.

Robinson, R. S., Mix, A., & Martinez, P. (2007). Southern Ocean control on the extent of denitrification in the southeast Pacific over the last 70ka. *Quaternary Science Reviews*, *26*(1), 201-212.

Rodrigo-Gámiz, M., Martínez-Ruiz, F., Rampen, S. W., Schouten, S., & Sinninghe Damsté, J. S. (2014). Sea surface temperature variations in the western Mediterranean Sea over the last 20 kyr: A dual-organic proxy (UK′ 37 and LDI) approach. *Paleoceanography*, *29*(2), 87-98.

Rodrigo-Gámiz, M., Rampen, W., Haas, H. D., Baas, M., Schouten, S., & Sinninghe Damsté, J. S. (2015). Constraints on the applicability of the organic temperature proxies UK'37, TEX86 and LDI in the subpolar region around Iceland. *Biogeosciences, 12,* 6573–6590

Schouten, S., Hopmans, E. C., Schefuß, E., & Damste, J. S. S. (2002). Distributional variations in marine crenarchaeotal membrane lipids: a new tool for reconstructing ancient sea water temperatures?. *Earth and Planetary Science Letters*, *204*(1), 265-274.

Schouten, S., Huguet, C., Hopmans, E. C., Kienhuis, M. V., & Sinninghe Damsté, J. S. (2007). Analytical methodology for TEX86 paleothermometry by high-performance liquid

chromatography/atmospheric pressure chemical ionization-mass spectrometry. *Analytical Chemistry*, *79*(7), 2940-2944.

Schouten, S., Hopmans, E. C., van der Meer, J., Mets, A., Bard, E., Bianchi, T. S., ... & Huguet, C. (2009). An interlaboratory study of TEX86 and BIT analysis using high-performance liquid chromatography–mass spectrometry. *Geochemistry, Geophysics, Geosystems*, *10*(3).

Schouten, S., Hopmans, E. C., & Damsté, J. S. S. (2013). The organic geochemistry of glycerol dialkyl glycerol tetraether lipids: a review. *Organic geochemistry*, *54*, 19-61.

Shackleton, N. J., Hall, M. A., & Vincent, E. (2000). Phase relationships between millennial-scale events 64,000–24,000 years ago. *Paleoceanography*, *15*(6), 565-569.

Shackleton, N. J., Sánchez-Goñi, M. F., Pailler, D., & Lancelot, Y. (2003). Marine isotope substage 5e and the Eemian interglacial. *Global and Planetary change*, *36*(3), 151-155.

Shackleton, N. J., Fairbanks, R. G., Chiu, T. C., & Parrenin, F. (2004). Absolute calibration of the Greenland time scale: implications for Antarctic time scales and for Δ 14 C. *Quaternary Science Reviews*, *23*(14), 1513-1522.

Shrivastava, M. K., Subramanian, R., Rogge, W. F., & Robinson, A. L. (2007). Sources of organic aerosol: Positive matrix factorization of molecular marker data and comparison of results from different source apportionment models. *Atmospheric Environment*, *41*(40), 9353-9369.

Sinninghe Damsté, J. S., Schouten, S., Hopmans, E. C., van Duin, A. C., & Geenevasen, J. A. (2002). Crenarchaeol the characteristic core glycerol dibiphytanyl glycerol tetraether membrane lipid of cosmopolitan pelagic crenarchaeota. *Journal of Lipid Research*, *43*(10), 1641-1651.

Sinninghe Damsté, J. S., Rampen, S., Irene, W., Rijpstra, C., Abbas, B., Muyzer, G., & Schouten, S. (2003). A diatomaceous origin for long-chain diols and mid-chain hydroxy methyl alkanoates widely occurring in Quaternary marine sediments: indicators for high-nutrient conditions. *Geochimica et Cosmochimica Acta*, *67*(7), 1339-1348.

Stott, L., Poulsen, C., Lund, S., & Thunell, R. (2002). Super ENSO and global climate oscillations at millennial time scales. *Science*, *297*(5579), 222-226.

Strub, P. T., Mesías, J. M., Montecino, V., Rutllant, J., & Salinas, S. 1998. Coastal ocean circulation off western South America. *Robinson, AR and K. Brink, H.(eds.), The Sea*, 273-313.

Thiel, M., Macaya, E. C., Acuna, E., Arntz, W. E., Bastias, H., Brokordt, K., ... & Dumont, C. P. (2007). The Humboldt Current System of northern and central Chile: oceanographic processes, ecological interactions and socioeconomic feedback. *Oceanography and marine biology*, *45*, 195-344.

Tudhope, A. W., Chilcott, C. P., McCulloch, M. T., Cook, E. R., Chappell, J., Ellam, R. M., ... & Shimmield, G. B. (2001). Variability in the El Niño-Southern Oscillation through a glacial-interglacial cycle. *Science*, *291*(5508), 1511-1517.

Verleye, T. J. (2011). The late Quaternary palaeoenvironmental changes along the western South-American continental slope: A reconstruction based on dinoflagellate cysts and TEX86. PhD Thesis. Ghent University: Gent. 245 pp.

Versteegh, G. J. M., Bosch, H. J., & De Leeuw, J. W. (1997). Potential palaeoenvironmental information of C 24 to C 36 mid-chain diols, keto-ols and mid-chain hydroxy fatty acids; a critical review. *Organic Geochemistry*, *27*(1), 1-13.

Volkman, J. K., Eglinton, G., Corner, E. D., & Forsberg, T. E. V. (1980). Long-chain alkenes and alkenones in the marine coccolithophorid Emiliania huxleyi. *Phytochemistry*, *19*(12), 2619-2622.

Volkman, J. K., Barrett, S. M., & Blackburn, S. I. (1999). Eustigmatophyte microalgae are potential sources of C 29 sterols, C 22–C 28 n-alcohols and C 28–C 32 n-alkyl diols in freshwater environments. *Organic Geochemistry*, *30*(5), 307-318.

Wang, C., & Picaut, J. (2004). Understanding ENSO physics—A review. *Earth's Climate*, 21-48.

Weber, Y., De Jonge, C., Rijpstra, W. I. C., Hopmans, E. C., Stadnitskaia, A., Schubert, C. J., ... & Niemann, H. (2015). Identification and carbon isotope composition of a novel branched GDGT isomer in lake sediments: Evidence for lacustrine branched GDGT production. *Geochimica et Cosmochimica Acta*, *154*, 118-129.

Willmott, V., Rampen, S. W., Domack, E., Canals, M., Sinninghe Damsté, J. S., & Schouten, S. (2010). Holocene changes in Proboscia diatom productivity in shelf waters of the north-western Antarctic Peninsula. *Antarctic Science*, *22*(1), 3.

Wuchter, C., Schouten, S., Wakeham, S. G., & Sinninghe Damsté, J. S. (2005). Temporal and spatial variation in tetraether membrane lipids of marine Crenarchaeota in particulate organic matter: implications for TEX86 paleothermometry. *Paleoceanography*, *20*(3).

Wuchter, C., Schouten, S., Wakeham, S. G., & Sinninghe Damsté, J. S. (2006). Archaeal tetraether membrane lipid fluxes in the northeastern Pacific and the Arabian Sea: implications for TEX86 paleothermometry. *Paleoceanography*, *21*(4).

Zhang, Y. G., Zhang, C. L., Liu, X. L., Li, L., Hinrichs, K. U., & Noakes, J. E. (2011). Methane Index: a tetraether archaeal lipid biomarker indicator for detecting the instability of marine gas hydrates. *Earth and Planetary Science Letters*, *307*(3), 525-534.